The Pennsylvania State University

The Graduate School

EXAMINING ASYMMETRIC PRECIPITATION PROCESSES AND VERTICAL WIND SHEAR IN TYPHOON NESAT (2017)

A Thesis in

Meteorology and Atmospheric Science

by

Katriella Tenembaum

Submitted in Partial Fulfillment
of the Requirements
for the Degree of

Master of Science

August 2023

The thesis of Katriella Tenembaum was reviewed and approved by the following:

Anthony C. Didlake, Jr.
Associate Professor of Meteorology
Thesis Advisor

Yunji Zhang
Assistant Professor
Assistant Director, Penn State Center for Advanced Data Assimilation and Predictability Techniques

Kelly Lombardo
Associate Professor of Meteorology and Atmospheric Science

David J. Strensrud
Professor of Meteorology
Head, Department of Meteorology and Atmospheric Science

ABSTRACT

Tropical cyclones (TCs) can produce heavy precipitation which can be difficult to predict. Asymmetric structures in TCs are prominent features, and understanding how these asymmetric precipitation patterns can form and vary is critical for forecasting TC rainfall. This study analyzes the characteristics and variability of precipitation asymmetries in TCs of different intensities using an ensemble model run of Typhoon Nesat (2017) that was run in preparation for the NSF PRECIP field campaign. Given that a TC's precipitation is affected by the environmental deep-layer vertical wind shear, further study of the effects of vertical wind shear on TC precipitation will be helpful in further elucidating the interactions between the asymmetry and the important precipitation forcing mechanisms. This work analyzes the processes and variability of shear/precipitation interactions in ensemble members that are divided into three groups of storm intensity. It is found that more intense storms tend to have lower shear magnitude and more precipitation before landfall and vice versa. While rain rates tended to be similar, the increase in precipitation before landfall is due to variations in the track trajectory as a result of the stronger storm intensities. In the eyewall the precipitation maxima tends to be left of shear, and for the rainbands it tends to be right of shear. This is due to the tilt of the vortex leading to potential temperature and potential vorticity anomalies leading to increased updrafts. Composites of the ensemble were examined and they support the previous conclusions and prior research.

TABLE OF CONTENTS

LIST OF FIGURES

ACKNOWLEDGEMENTS

This material is based upon work supported by the NSF under Award NSF Grant AGS-1854607. Any opinions, findings, and conclusions or recommendations expressed in this publication are those of the author and do not necessarily reflect the views of the NSF.

Thanks to Anthony Didlake for advising, assistance and support. Thanks to Yunji Zhang for providing the model data. Thanks to Nicholas Barron, for his assistance with various aspects of coding.

Chapter 1

Introduction

Tropical cyclones (TCs) are deadly and costly natural phenomena that affect many regions across the world. The socioeconomic impact from TCs is caused by a variety of factors, such as storm surge, rain, winds, tornadoes, and marine incidents. The heavy rainfall in TCs can cause destructive events such as flooding and mudslides. Rainfall and its associated flooding and mudslides account for 27% of TC deaths, making it the second leading cause of death in U.S. Atlantic TCs (Rappaport, 2014). Predicting TC rainfall location, timing, and intensity is important to help avoid such deaths in the future.

Extreme rainfall is especially hard to predict accurately even outside of a TC environment. The threat score, a metric for determining accuracy of forecasts with 0 being no skill and 1 being perfect skill, was less than 0.25 for U.S. rainfall events with a 2 in/day threshold in 2011. When looking at the top 0.1% of events, the threat score was less than 0.2 (Sukovich et al., 2014). A major cause of this poor skill in heavy rainfall prediction is that the resolution of weather forecast models is coarser than the scales upon which cloud microphysical and precipitation processes happen (Morrison et al., 2020). The coarse resolution in models requires that said processes be parameterized. But such parameterizations are imperfect, and errors in microphysics parameterization schemes lead to errors in the model simulations and thus in the forecasts. These issues all exist in TC modeling, which results often in poor heavy rainfall forecasts for TCs. Improved understanding of the dynamics and the modeling of TC precipitation is necessary to mitigate damage from the rainfall.

The heaviest precipitation in a TC typically occurs in the eyewall. Here, the precipitation is dominated by warm rain processes (Houze, 2010; Marks & Houze, 1987). The precipitation primarily follows two main trajectories as outlined by Marks and Houze (1987); one for larger hydrometeors and one for smaller hydrometeors. The large hydrometeors are associated with convective processes and form in the eyewall updraft, grow via warm rain processes, and travel short distances before falling out still in the eyewall. The smaller hydrometeors that begin in the eyewall updraft travel long distances around the eyewall and are advected out via the upper layer outflow. These hydrometeors grow largely through stratiform processes and eventually fall out outside of the eyewall in regions where stratiform precipitation dominates.

The convective precipitation in the eyewall of a TC is usually asymmetric due to the storm motion and the vertical wind shear of the environment (e.g., Bender, 1997; Corbosiero & Molinari, 2003; Houze, 2010). TC movement causes convergence at the front of the storm which causes air to rise and rain to fall (Shapiro, 1983). Vertical wind shear will have a stronger impact on the location of the rainfall asymmetry than storm motion in cases of strong shear (>7.5 ms^{-1}) (Chen et al., 2006; Yang et al., 2016). TCs in strong vertical wind shear tend to be more asymmetric than those in weak vertical wind shear (Reasor et al., 2013).

Environmental vertical wind shear, for this study defined as the 850 – 200 hPa vertical wind shear in the environment 800 km away from the storm center, has a large impact on the structure of tropical cyclones and can cause significant asymmetries. The wind structure of a TC is affected by the wind shear, with updrafts being more common downshear and downdrafts upshear. There are two theories for why this occurs. Vertical wind shear causes the vortex to tilt in the direction slightly left of the shear vector. This tilting creates a potential temperature wavenumber-1 asymmetry, with elevated potential temperature uptilt, and lower potential

temperature downtilt. As air flows tangentially around the storm along constant lines of potential temperature, this air rises upward going from the positive to the negative anomaly in the downshear-right region, and vice versa (Braun et al., 2006; Dehart et al., 2014; Frank & Ritchie, 1999; Jones, 1995). The second theory is based on differential vorticity advection. The radial flow in the boundary layer and upper troposphere exhibit a wavenumber-1 asymmetry due to the wind shear, which then advects the vorticity towers of the eyewall differently relative to the shear direction. This process yields rising motion downshear and sinking motion upshear (Bender, 1997; Black et al., 2002; Frank & Ritchie, 2001). The eyewall precipitation maxima can usually be found left-of-shear as the rain generated by updrafts downshear is advected around the storm (Black et al., 2002; Chen et al., 2006; Feng & Bell, 2019; Uhlhorn et al., 2014; Xu et al., 2014). This maximum usually occurs one quadrant downwind of the convection generation (Hence & Houze, 2011). As vertical wind shear shifts direction, the location of the wavenumber-1 asymmetry can shift with it (Yu et al., 2015).

Moving out from the eyewall, rainbands under sufficiently strong wind shear can form a Stationary Band Complex (SBC; Willoughby et al., 1984), that is organized relative to the wind shear vector (Chen et al., 2006; Hence & Houze, 2012; Riemer, 2016). The SBC forms at the boundary between the high equivalent potential temperature air of the core and the relatively lower equivalent potential temperature air of the environment. Vertical wind shear leads to low-level asymmetries in the equivalent potential temperature and vorticity (e.g., Jones, 1995) with higher values to the right of the shear vector, leading to convection amplification downshear right (Riemer, 2016). Within the SBC, newer convection forms in the right-of-shear side, while older stratiform precipitation dominates the left-of-shear side (Didlake & Houze, 2013; Didlake & Kumjian, 2017; Hence & Houze, 2012).

The Prediction of Rainfall Extremes Campaign In the Pacific (PRECIP) was a field campaign funded by the National Science Foundation (NSF) with the goal to improve understanding and prediction of extreme rain processes of various forms, including TCs, in southeast Asia. PRECIP had a modeling component to investigate the predictability of the observed weather systems. Taiwan was chosen because it has a moisture-rich environment, complex terrain, and an oceanic environment, which all contribute to a high frequency of heavy rainfall events. Due to the considerable amount of rain Taiwan gets, even non-extreme amounts of rainfall would likely be considered extreme elsewhere in the world (Wu et al., 2017). Rainfall accumulation depends on both the intensity and duration of the rainfall, and can be represented

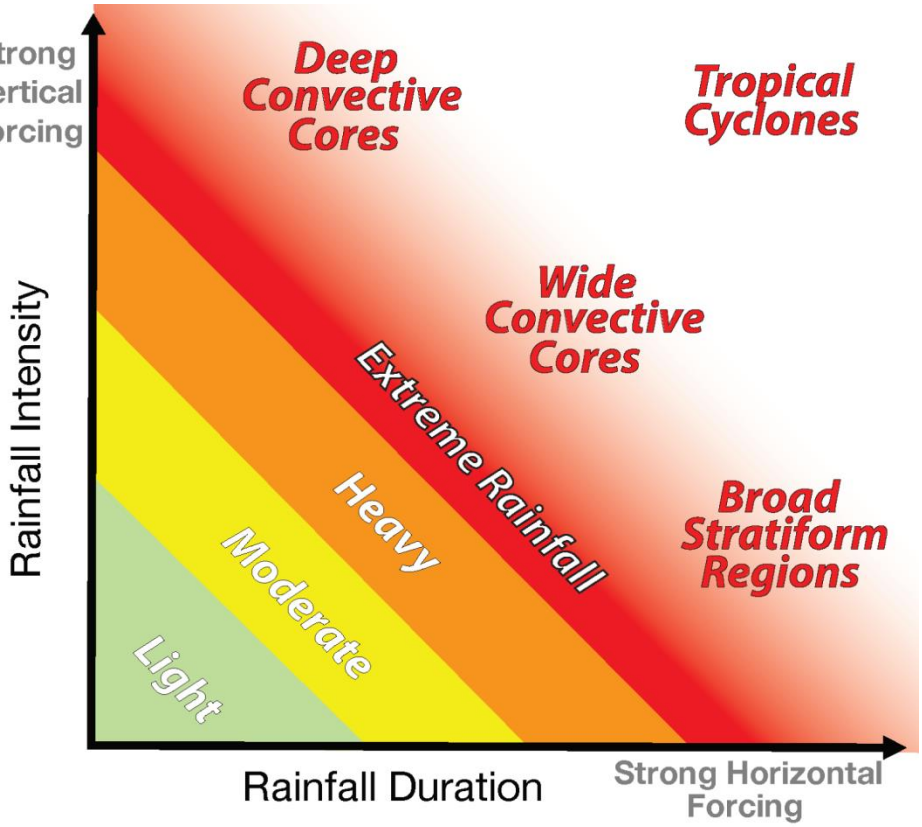

Figure **1-1**: Rainfall accumulation phase space. (PRECIP 2022 Science, n.d.)

by the equation R = I * D put forth by Doswell et al. (1996), where I is rainfall rate, D is rainfall duration, and R is total accumulated rainfall. In order to get extreme rainfall a high rainfall rate, a long duration, or a combination thereof is needed, as shown in Figure 1. Duration is determined by horizontal forcing and intensity is determined by vertical moisture flux and precipitation efficiency. The modeling portion of PRECIP will assist in determining if the primary forcing mechanisms for extreme rainfall are due to unique dynamic or thermodynamic processes, or some combination thereof.

Given that extreme precipitation in TCs is affected by the vertical wind shear, further study of the effects of vertical wind shear on TC precipitation should be helpful in further elucidating the interactions between the asymmetry and the precipitation mechanisms which are not fully understood. This work looks at the effect that relatively small changes in shear can have on TC intensity and precipitation by looking at an ensemble model run of Typhoon Nesat (2017) that was run as a dry run test case prior to PRECIP in order to test the setup prior to the campaign. An ensemble model approach allows for differences in the same TC to be compared, while still having a base of comparison, i.e., same model, similar initial conditions. It provides forecast uncertainties and a probabilistic approach. A high-resolution model simulation of Typhoon Nesat (also called Gorio in the Philippines) will be examined as a case study of TC precipitation in a sheared environment. Typhoon Nesat was a category 2 storm that made landfall in Taiwan and China on July 29, 2017. Nesat strengthened as it approached landfall in Taiwan before beginning to dissipate as it crossed Taiwan's mountains. Nesat then made landfall in China as a tropical storm.

The goal of this work is to analyze the characteristics and variability of shear-aligned precipitation asymmetries in TCs of different intensities. This work uses an ensemble model run

of Typhoon Nesat (2017), that was run in preparation for the PRECIP field campaign, and analyzes the processes and variability of shear/precipitation interactions in ensemble members that are divided into three intensity groups. This examination will be helpful in further elucidating the sensitivity of forcing mechanisms of TC precipitation asymmetries, which will in turn lead to an improved understanding of the dynamics and improved modeling and forecasting of TC precipitation.

Chapter 2

Methods

The model used in this study is the Pennsylvania State University Weather Research and Forecasting Model - Ensemble Kalman Filter (PSU WRF-EnKF), which combines the Weather Research and Forecasting (WRF) Model – Advanced Research WRF v 4.1.3 (Skamarock et al., 2019), the ensemble square root filter (EnSRF; Houtekamer & Mitchell, 2001) variation of EnKF, and the Community Radiative Transfer Model (CRTM; Han et al., 2006), version 2.3.0. It was run with two nested domains: an outer domain with a horizontal grid spacing of 9 km for a total size of 3,600 km by 4,050 km, and a one-way nested inner domain with a horizontal grid spacing of 3 km for a total size of 900 km by 900 km, covering Taiwan and surroundings with hourly output. The model has 50 vertical levels. The suite of model physics includes the Thompson aerosol-aware microphysics scheme (Thompson & Eidhammer, 2014) which was shown to have high accuracy in TCs by Brown et al. (2016), the Yonsei University (YSU) boundary layer scheme (Hong et al., 2006), the revised MM5 Monin-Obukhov scheme for surface layer processes (Jiménez et al., 2012), the Noah land-surface model (Tewari et al., 2004), and the Rapid Radiative Transfer Model for GCM (RRTMG) scheme for longwave and shortwave radiations (Iacono et al., 2008). No cumulus scheme was used. The model was initialized using assimilated data from all available conventional observations, minimum sea level pressure of Nesat from the best-track estimations of the Japan Meteorological Agency (JMA), and all-sky infrared brightness temperatures from channel 10 of the Japanese

Himawari-8 geostationary satellite. The model has 60 ensemble members and was run for 24 hours covering the period of 00 UTC 29 July 2017 to 00 UTC 30 July 2017.

This study focuses on the high-resolution inner domain. Vertical wind shear was calculated using the method from Davis et al. (2008) where first, the irrotational and nondivergent components of the wind are subtracted from the 200 and 850 hPa horizontal wind fields. Next, the background flow is averaged over a disk centered at the storm center and extending outward 800 km; then the 850 hPa vector is subtracted from the 200 hPa vector in order to obtain the shear vector. The storm centers were found using the pressure centroid method outlined in Nguyen et al. (2014).

The ensemble simulations were sorted into three categories based on intensity, which likely impacts precipitation structure and amounts. Average minimum central pressure prior to landfall was used to determine the three categories: Strong, Medium, and Weak. Several TC parameters were examined by this intensity categorization.

Chapter 3

Overview of Actual and Simulated Storm

The time under consideration in this study is 00 UTC 29 July 2017 to landfall, which for the actual storm was 12 UTC 29 July 2017 according to the International Best Track Archive for Climate Stewardship (IBTrACS; Knapp et al., 2010; Knapp et al., 2018). Figure 3-1 shows the tracks, maximum windspeed, minimum central pressure, shear direction, and shear magnitude for the actual storm, model ensembles, and ensemble mean. During this time period, Nesat's maximum sustained winds were 80 knots (~41 ms^{-1}) (averaged over 10 minutes at 10 m) and the minimum central pressure was 960 mb (Figure 3-1) though the IBTrACS dataset only has three and six hourly data so the shorter time scale features are unlikely to be visible. The minimum central pressure is very close to the ensemble mean. The observed maximum sustained winds are lower than the model-predicted maximum winds shown in Figure 3-1. This is likely because the IBTrACS data are 10-minute sustained winds at 10 meters and not the highest unsustained winds at any height. No gust measurements exist for this time period. When looking at WRF's 10 m winds for Nesat (not shown) the ensemble mean throughout this time varies from 35 to 40 ms^{-1}, just a bit lower than the IBTrACS estimate. Nesat moved northwest during this time period making landfall in Yilan County in northeast Taiwan. This track is further north than the ensemble mean, though a few of the northernmost members show a similar landfall location.

The ensemble model run of Typhoon Nesat is analyzed only for the times prior to landfall since the Central Mountain Range of Taiwan caused Nesat to weaken substantially. The ensemble members are moving northwest towards Taiwan. The maximum windspeeds and pressure indicate that the storms tend to weaken initially before levelling out. This overall

weakening in the beginning corresponds with an increase in the vertical wind shear, consistent with the expected impacts of stronger vertical wind shear (e.g., Frank & Ritchie, 2001; Wong & Chan, 2004). Vertical wind shear is strong (10 ms^{-1}) in most ensemble members (Figure 3-1b), so clear asymmetries in the eyewall and larger precipitation field are expected in the simulated TCs (Reasor et al., 2013; Chen et al., 2006). Weaker TCs tend to be more susceptible to shear-induced asymmetries (Xu et al., 2014), so as the storm initially weakens it should be more asymmetric than later on when the intensity remains level, not accounting for the effects of landfall.

The shear direction is generally constant with a mean of 199° (i.e., shear vector pointing to the southwest) (Figure 3-1e). The storm motion varies from west to north-northwest consistent with the southeasterly prevailing winds typical to the southwest of the western Pacific sub-tropical high in this region. This places the storm motion vector to the right of the shear vector and the maximum precipitation to the rear of the storm consistent with Yang et al. (2016). This is different from the general North Atlantic pattern, which places the storm motion vector to the left of the shear vector and the convection maxima downmotion right consistent with Shapiro's (1983) storm motion effect (Corbosiero & Molinari, 2003). However, the direction of the storm motion should have little effect as strong shear dominates the asymmetries regardless of the angle between the shear vector and the motion of the TC (e.g. Corbosiero & Molinari, 2003; Chen et al., 2006; Uhlhorn et al., 2014; Yang et al., 2016).

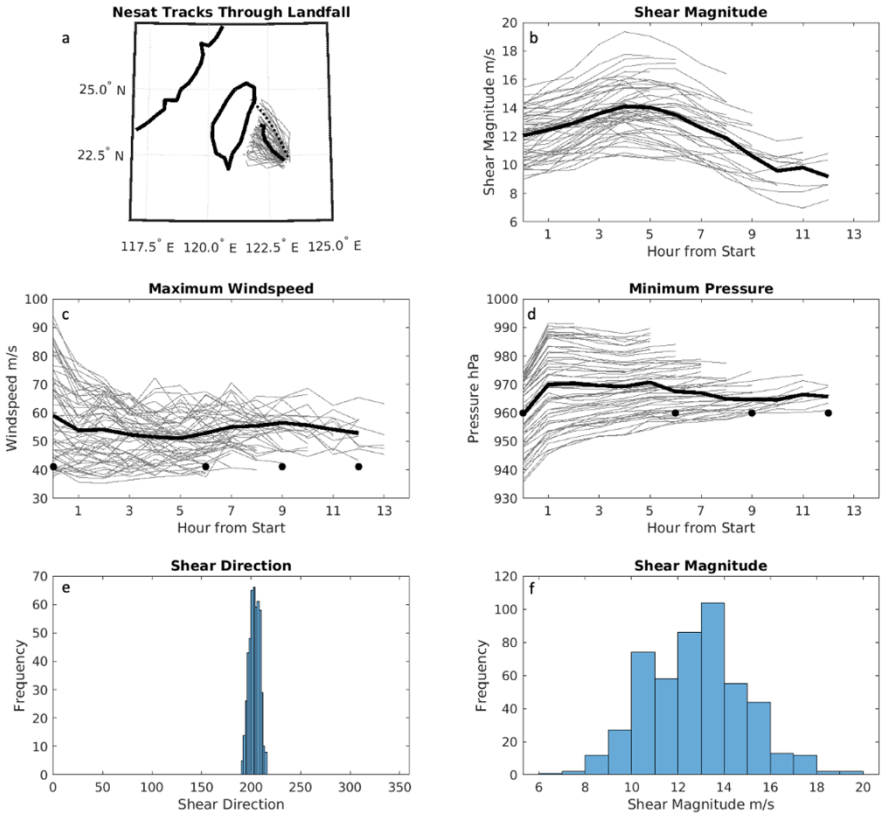

Figure **3-1**: a: track of ensemble members prior to landfall on a map showing the domain of the model. Bold black line = ensemble mean. Dotted line = IBTrACS track, b: Shear magnitude of ensemble members over time prior to landfall. Bold black line = ensemble mean. c: same as b but for maximum windspeed. Black circles = IBTrACS intensity d: same as c but for minimum central pressure. e: Histogram of shear direction prior to landfall for all ensemble members. f: Histogram of shear magnitude prior to landfall for all ensemble members.

Chapter 4

Results

Intensity Relative Analysis of Ensemble

We sorted our ensemble members into three intensity categories based on mean minimum central pressure prior to landfall: Strong, Medium, and Weak. This separation allows us to examine differences that are expected based on prior research showing that more intense storms are more resistant to vertical wind shear asymmetries (e.g. Xu et al., 2014) and tend to have higher rainfall rates (e.g. Lonfat et al., 2004). The 20 members with the lowest mean minimum central pressure are categorized as Strong, the highest 20 members as Weak, and the middle 20 members as Medium. Figure 4-1 shows the maximum windspeed, minimum central pressure, track, and shear magnitude of the ensemble members for each category. Once separated into intensity categories, a few patterns emerge. The minimum pressures over time for each category are well separated with very slight overlap, showing that the ensemble members generally keep their relative minimum central pressure over time. There is a clear connection to windspeed as expected (Figure 4-1c) - the maximum windspeed is highest for the Strong category members and lowest for the Weak category members. The means of each category maintain the pattern. Vertical wind shear is generally greater in the Weak cases and lesser in the Strong cases (see Figure 4-1). This relationship between shear magnitude and intensity is expected as strong shear inhibits storm development (e.g. DeMaria, 1996; Gray, 1968; Merrill, 1988; Gu et al., 2015). When looking at the storm tracks, Weak cases tend to move more westward while Strong cases

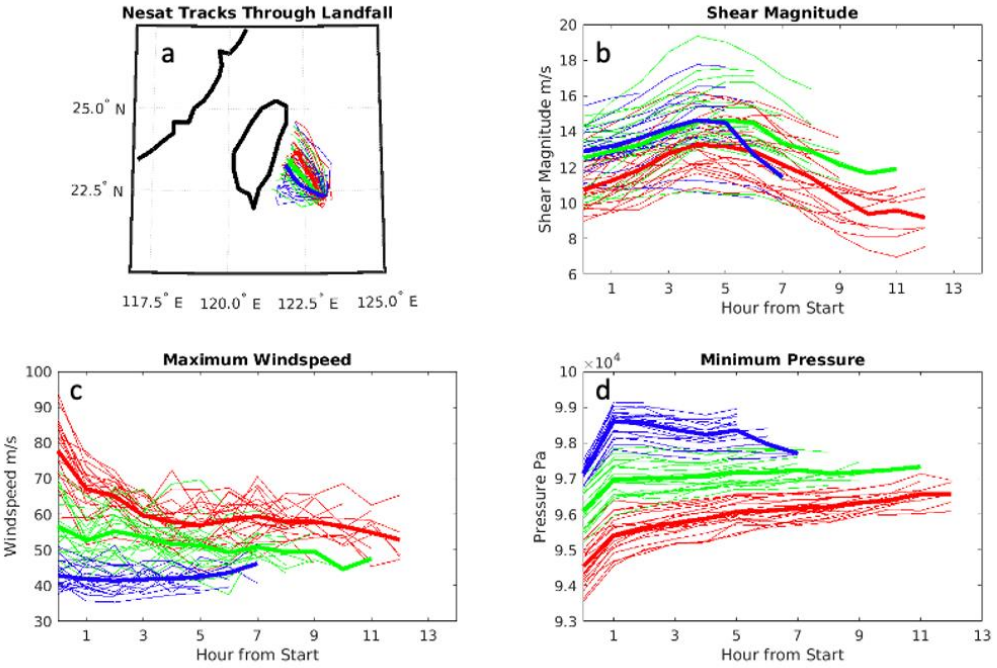

Figure **4-1**: a: Track prior to landfall grouped by mean minimum central pressure. Red = Strong, Green = Medium, Blue = Weak. Bold lines indicate category mean. b: Shear magnitude over time grouped by minimum pressure. c: Same as b but for maximum windspeed. d: Same as b but for minimum central pressure.

move more northward. In addition, the Strong cases generally take more time to reach landfall given the track trajectories and the geometry of the Taiwan coast. The mean landfall time for the Strong cases is 11.9 hours, 9.2 hours for the Medium cases, and 6.5 hours for the Weak cases. The track differences may be due to two possible reasons. β-drift causes Northern Hemispheric storms to drift northwestward, and the more intense storms move more to the north on average (Chan & Williams, 1987; Wang & Li, 1992; Wang & Holland, 1996). Orographic effects can also impact the track. As TCs approach Taiwan's Central Mountain Range, which reaches 3 km in altitude, the storms often deflect to the north or south depending on the approach trajectory

and storm structure (e.g. Bender et al., 1987; Yeh & Elsberry, 1993; Wu, 2001; Huang et al., 2016; Huang et al., 2019). The tracks that move northward are more consistent with Nesat's actual track[1].

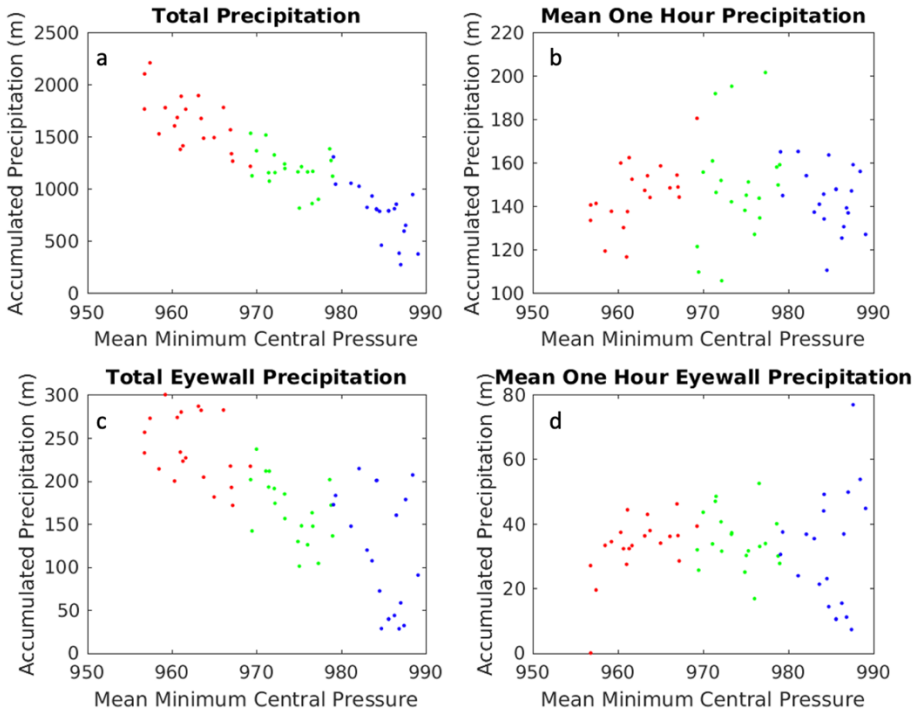

Figure **4-2:** a: Total accumulated precipitation prior to landfall across the whole domain for each ensemble member grouped by mean minimum central pressure. Red = Strong, Green = Medium, Blue = Weak. b: Mean one hour precipitation accumulation prior to landfall across the whole domain for each ensemble member grouped by mean minimum central pressure. c: Same as a but for eyewall precipitation only. d: same as b but for eyewall precipitation only.

Storm intensity also correlates with the precipitation of the storm. Figure 4-2 shows the storm precipitation for each intensity group. The total accumulated precipitation prior to landfall

[1] Huang et al. (2019), discusses Nesat's deflection in more detail.

shows a clear negative correlation with mean minimum central pressure, wherein the strongest storms produce the greatest rainfall. In contrast, when looking at the one-hour accumulated precipitation averaged from start to landfall, there is no clear connection to intensity. Given that the Strong TCs tend to take longer to reach landfall and thus have a longer duration under consideration, the time of this analysis duration determines the total precipitation accumulated rather than the precipitation rate. We next focus on solely the eyewall precipitation given that TC eyewalls tend to have higher rain rates than the rainbands (Lonfat et al., 2004; Yu et al., 2017). For the purpose of this work the eyewall is taken as an annulus centered around the radius of maximum winds (RMW) and 18 km to either side of the RMW, due to this annulus adequately encompassing the eyewall precipitation at all times for each member. The total accumulated eyewall precipitation shows a similar, though less well defined, correlation as the total accumulated precipitation, with Strong TCs having more accumulated rainfall and Weak TCs having less accumulated rainfall. There is no clear connection between the intensity and the mean one-hour accumulated precipitation, though there is more variability in the mean one-hour eyewall precipitation for weak TCs than for either of the other categories. The lack of connection between the intensity and the one-hour accumulated precipitation (rain rate) is counter to previous studies (e.g. Lonfat et al., 2004; Yu et al., 2017) which showed that more intense TCs had higher rain rates. The more intense TCs do have more total accumulated rain due to the longer duration prior to landfall rather than having higher rain rates as would have been expected. This connection between duration and total accumulated precipitation is true for the eyewall as well as for the total domain.

Shear Relative Analysis of Eyewall Precipitation

The location of maximum precipitation in the eyewall tends to be dependent on the direction of the environmental wind shear vector. Figures 4-3a and b show the azimuth angles and shear-relative angles of maximum eyewall precipitation for all timesteps of the ensemble members prior to landfall. The location of maximum precipitation in the eyewall was found via computing a radial average of the one-hour accumulated precipitation for the eyewall annulus described previously. The azimuth of the maximum annulus-averaged precipitation was determined for all 60 ensemble members prior to landfall. Overall, the angle of maximum

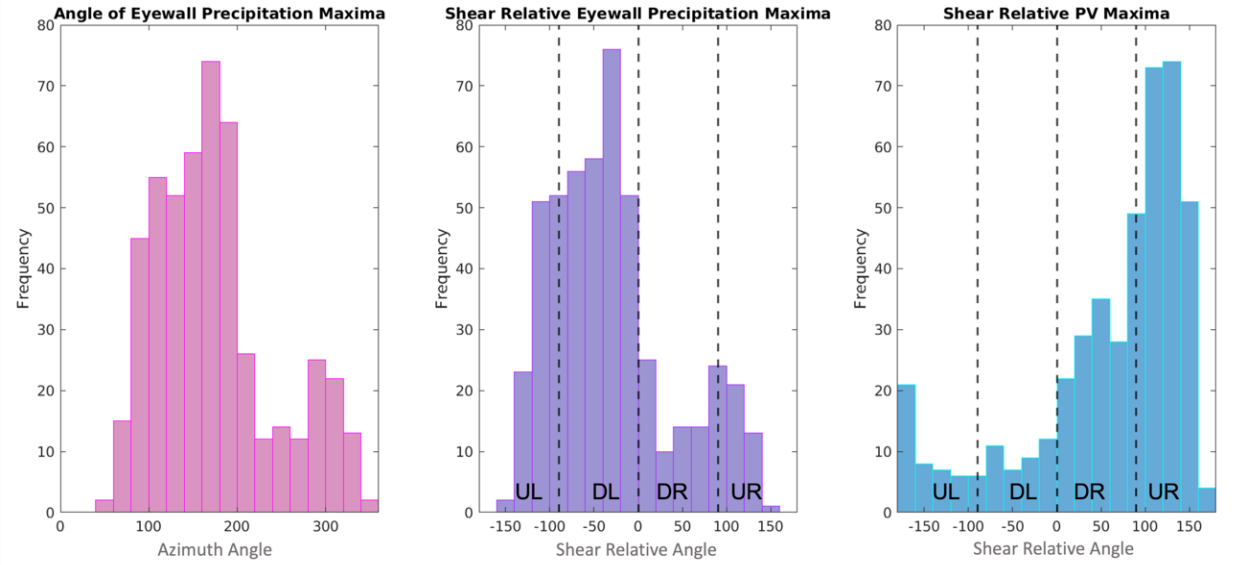

Figure **4-3**: a: Histogram of azimuth angle of eyewall precipitation maxima prior to landfall in meteorological angles. b: Histogram of angle of eyewall precipitation maxima prior to landfall relative to shear. Shear quadrants marked by UL (upshear left), DL (downshear left), DR (downshear right), and UR (upshear right). c: Angle of maximum low-level PV relative to shear.

precipitation is approximately between -100°–0° shear-relative azimuth, which is left of the shear vector (see Figure 4-3). Having the maximum precipitation left-of-shear is consistent with Yu et al. (2015) and Yang et al. (2016); whereas according to DeHart et al. (2014), the maximum precipitation should, on average, be more downshear rather than so far left-of-shear. This discrepancy may be due to the different ocean basins with their differences in environmental flow, and the proximity to land. This peak left-of-shear is strongest at early hours in the ensemble (see Figure 4-4). There is a minor peak at approximately 300° (or to the northwest) evident in 4-3b primarily composed of later times (see Figure 4-4) and is likely caused by interactions with the mountains in the northwest where upslope flow will be strongest. Figure 4-5a and b demonstrates the change in angle. At the beginning of the simulation, the angle of maximum eyewall precipitation is to the southeast (upshear left). At the approach to land the angle of maximum precipitation shifts to the northwest as the eye interacts with the mountains

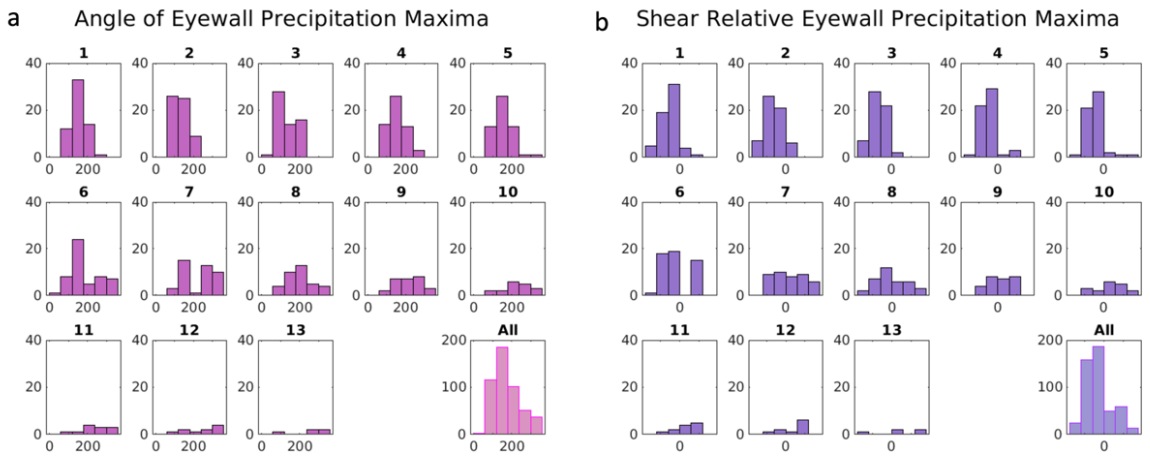

Figure **4-4**: a: Histograms of angle of eyewall precipitation maxima before landfall over time (each subplot is a timestep). Final subplot titled “All” is the same as Figure 4-1a with bin sizes matched to the rest of the subplots. b: Same as a but for shear relative angle and “All” subplot is the same as Figure 4-1b.

of Taiwan. The hours leading into landfall in the various ensemble members, 7 - 12Z, have much less distinct distributions than early hours, likely due to the mountains in Taiwan providing an additional strong source of asymmetry (e.g. Houze, 2012; Smith et al., 2009), combined with having fewer ensemble members remaining to be counted, leading to less robust statistics.

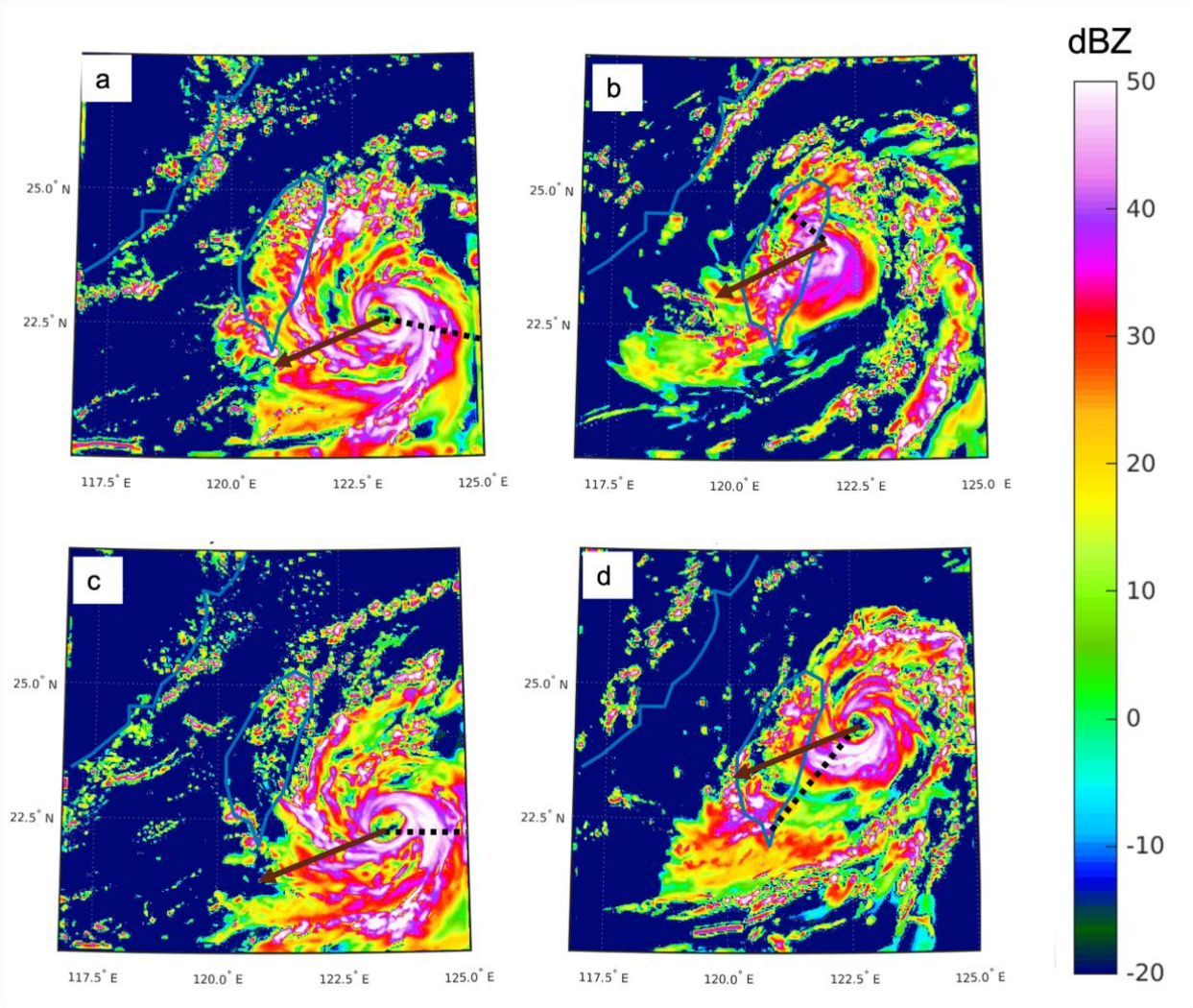

Figure **4-5**: (Preceding page) Plan views of two ensemble members of 2 km reflectivity of Typhoon Nesat. a: plan view of ensemble member 16 at hour 2 of simulation with black dashed line representing angle of maximum eyewall precipitation and brown arrow shear direction. b: same as a but at the hour just before landfall. c: same as a but for ensemble member 4 and angle of maximum outer precipitation (method 2). d: same as c but for the hour just prior to landfall.

We also analyze the potential vorticity (PV) asymmetry in the eyewall of the ensemble members. Ertel's Dry PV is defined as follows: $PV = \frac{1}{\rho}\zeta_a \cdot \nabla\theta$, where ρ = density, ζ_a= absolute vorticity, and θ = potential temperature. As such the PV maximum is dependent on vorticity and potential temperature. Figure 4-3c shows the shear-relative angle of the vertically-averaged (2-8 km) PV maxima, which largely occurs in the upshear-right quadrant. This location is consistent with larger PV values occurring in the lower tropospheric half of a sheared and tilted eyewall. When experiencing shear, a non-precessing eyewall tends have a steady-state tilt towards the downshear-left (downtilt direction), which means that the bottom of the eyewall juts into the upshear-right direction (uptilt). According to previous studies on the impacts of vortex tilt (Jones, 1995; Boehm & Bell, 2021; Frank & Ritchie, 1999), a tilted eyewall creates a low-level enhanced vorticity anomaly in the uptilt direction. Additionally, this vortex tilt leads to temperature anomalies in order to maintain thermal wind balance. These anomalies are a warm anomaly uptilt and a cold anomaly downtilt. The warm anomaly uptilt would bring larger potential temperature surfaces (isentropes) downward, compressing the surfaces and increasing its vertical gradient in the lower tropospheric half. The combination of the positive vorticity

anomaly and increased $\frac{\partial \theta}{\partial z}$ would cause the higher PV maximum in the uptilt, upshear-right direction. Air flowing around the eyewall along a constant isentrope would then rise moving from the warm to the cold anomaly largely in the downshear-right quadrant. The precipitation maxima tends to be left-of-shear, nearly directly opposite the PV maxima as air rises between the PV maxima and minima and precipitation falls out downwind.

The shear direction, magnitude, shear relative angle of maximum eyewall precipitation, and PV maxima as sorted into the intensity categories are shown in Figure 4-6. The shear direction shows a slight separation by intensity categories. While all shear directions are largely pointing to 199° azimuth (south-southwest), the Strong cases point slightly more to the west, while the Weak cases point slightly more to the south. As noted earlier, the Strong cases have weaker shear while the Weak cases have larger shear overall as expected given that shear, especially magnitudes greater than 10 ms^{-1}, is generally a well-known hindrance on TC intensity. The angle of maximum eyewall precipitation is further shear-left for the Strong cases. This is likely due to the higher winds advecting the hydrometeors further around the eyewall before they fall out. According to Wingo and Cecil (2010), higher shear magnitude shifts the precipitation maxima further left. However, Figure 4-6 shows that the Strong cases have the lowest shear magnitude while having their precipitation fall furthest left of shear. This may be due to the Nesat ensemble having what Wingo and Cecil classify as high shear (>10 ms^{-1}) for the majority of cases, so their results do not reflect differences within high shear. The PV maxima tend to be upshear-right (see Figure 4-6) with no clear differences between each category. The Strong cases have more maxima occurrences, particularly in the left-of-shear half, which implies that the tilt varies more frequently relative to the wind shear vector for the Strong cases. A tilt that varies its direction frequently is likely to be a weaker tilt. It is consistent that the Strong cases have a

weaker shear and thus a weaker tilt that has a wider range of shear-relative pointing directions compared to that of the Weak and Medium cases.

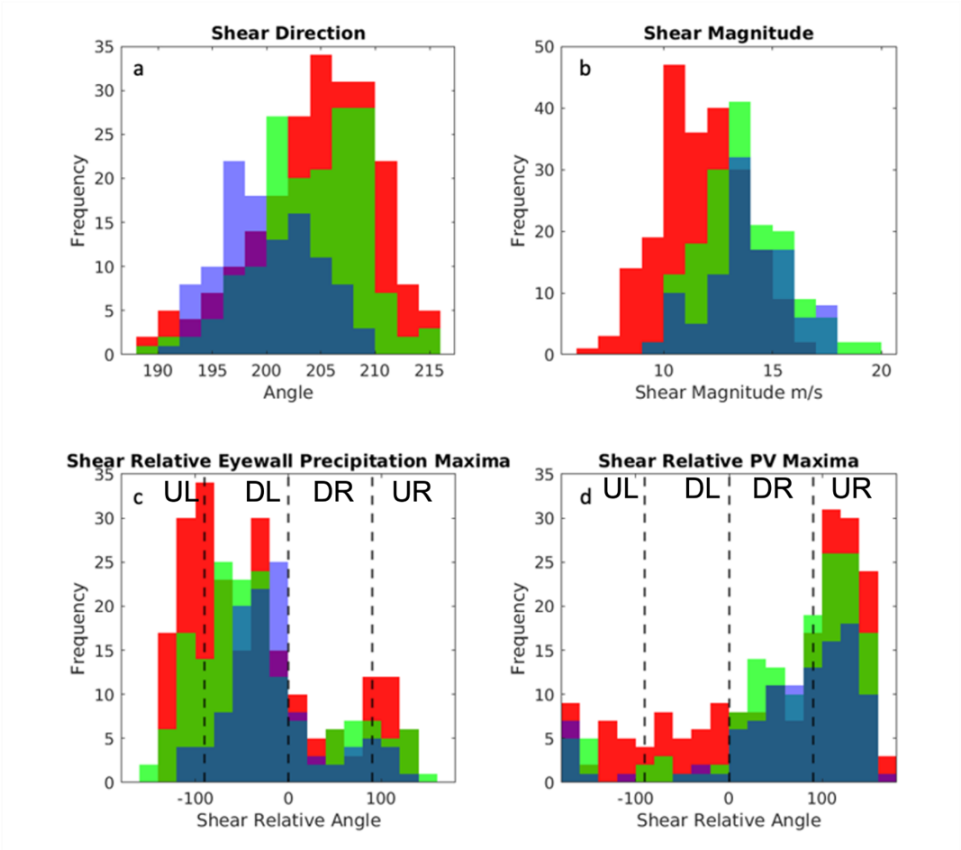

Figure **4-6**: a: Histogram of shear direction in degrees prior to landfall grouped by pressure. Red = Strong, Green = Medium, Blue = Weak. b: Same as top left but for shear magnitude in ms^{-1}. c: Same as figure 4-3b grouped by pressure. c: Same as figure 4-3c grouped by pressure.

Shear-Relative Analysis of Rainband Precipitation

In addition to looking at the eyewall precipitation maxima, the variability of shear-aligned asymmetries in the rainband precipitation is examined for different intensity groups because while much of the rainfall falls in the eyewall, a significant amount falls in the rainbands and should not be discounted when analyzing TC precipitation. The azimuth angle of the maximum precipitation in the rainband regions outside of the eyewall was calculated in a similar manner as the eyewall precipitation maxima but with two different approaches. Instead of averaging over an annulus centered on the RMW, the precipitation was averaged from the end of the eyewall (i.e., RMW +18 km) to the end of the domain (method 1) and from the end of the eyewall out to RMW +165 km which was the closest to the edge of the domain possible for the storms with the widest eyewall (method 2). Both methods were performed so that the domain's entire precipitation could be analyzed even though at some points the TCs' edges were not in the domain and to have a comparison with a controlled area so as to not have bias from having the precipitation maxima be biased due to there being more area for the precipitation to be averaged over when calculating the angle of maximum precipitation.

Figures 4-7, 4-8, 4-9, and 4-10 show these results for both methods of finding the maxima, and they produce similar results. Figure 4-7 shows the angle of rainband precipitation maxima using method 1 both in true azimuth and shear-relative coordinates, for the whole ensemble prior to landfall and split up into each timestep. The azimuth angle of maximum precipitation is generally between 100° and 280° and is fairly consistent through time though the exact location of the peak shifts around within those bounds. These angles are largely downshear

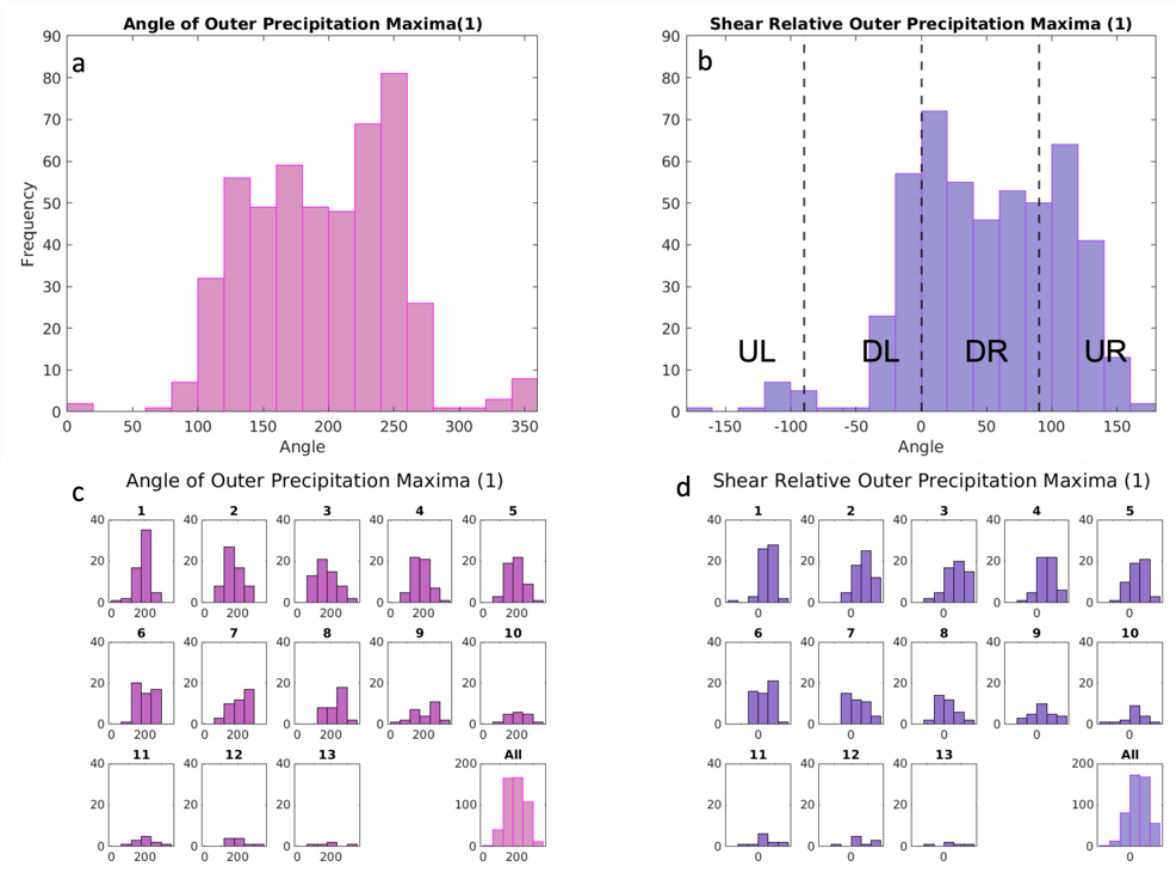

Figure **4-7**: a: Histogram of angle of outer precipitation maxima (1) before landfall. b: Histogram of shear relative angle of outer precipitation maxima (1). c and d: Same as Figure 4-4 but for outer precipitation maxima (1).

and right-of-shear. Method 1 includes both inner and outer rainbands, as defined by Hence and Houze (2012) and Corbosiero and Molinari (2002). They found that more precipitation occurred downshear-left for inner rainbands and downshear-right for outer rainbands. Hence and Houze (2012) found that the outer rainbands were more convective and less stratiform than the inner rainbands, and that upshear-right is the preferred convection genesis location, leading to the precipitation maxima downshear right. This is due to the shear induced tilt's creation of a region of enhanced vorticity and enhanced low level moisture overlapping (Riemer, 2016). The

preference for DR and UR in Figure 4-7 suggests that for Nesat the outer rainbands are more prominent than the inner rainbands. It is also possible that the shear-relative placement for convection in the rainbands is different for ocean basins, but this is not particularly likely as Wingo and Cecil (2010) did not find one. It can also be explained by the proximity of Taiwan; the rainbands that have already made landfall cause the location of maximum precipitation to shift further shear-right as the rainbands hit the mountains and rain out before being advected around the storm to shear-left.

Figure 4-8 shows the same information as Figure 4-7 but with the data split up into the Strong, Medium, and Weak categories. Here, an interesting pattern emerges. The Strong and Medium cases have a bimodal distribution with peaks downshear and upshear-right, while the Weak cases have their singular peak downshear-right. This bimodal distribution is largely indicative of the shear-relative maxima shifting directions over time. The earlier times have more maxima in the right-of-shear and upshear directions, while the later times have more maxima downshear. An example of this shift is shown in Figure 4-5c and d, where the maximum rainband precipitation shifts from the east to the southwest. This shift is likely caused by the TC flow interacting with the mountains near landfall. Specifically, as the typhoon approaches the island, the northwesterly flow on the southwest side increases and encounters the mountains that are oriented in the northeast-southwest direction. This near-perpendicular interaction creates a localized maximum in outer rainband precipitation.

The tracks for the Weak cases are more directly westward, which causes north-northeasterly winds to be the first interaction with the mountain range as the storm approaches. This flow is more parallel to the mountain range and thus does not produce orographically-induced outer precipitation maxima with the same frequency. So the precipitation maxima

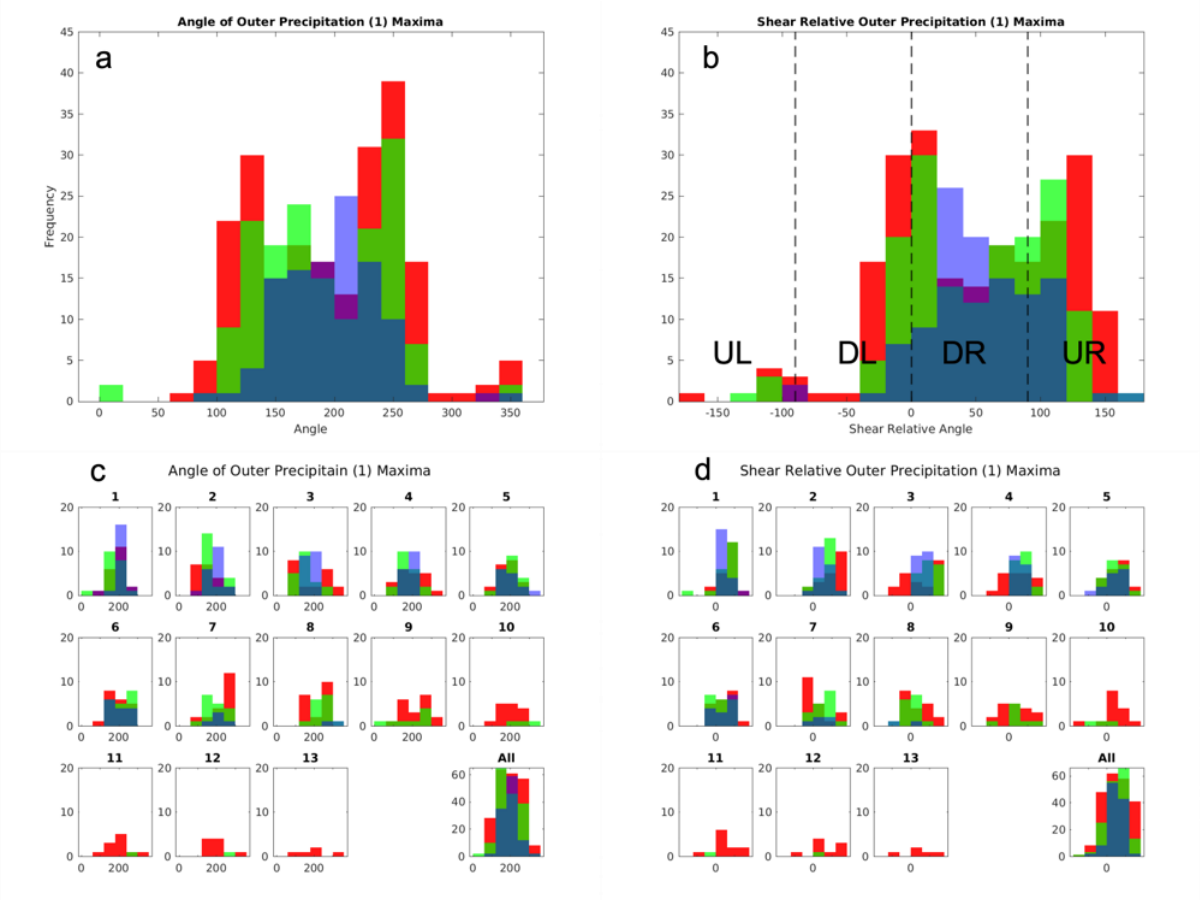

Figure **4-8**: Same as Figure 4-7 but separated by intensity. Red = Strong, Green = Medium, Blue = Weak.

frequency has a single-mode right-of-shear distribution that is consistent with shear-induced precipitation processes.

The overall results with method 2 are similar to method 1 as can be seen in Figures 4-9 and 4-10 which show the angle of maximum outer precipitation calculated via method 2. For method 2, the bimodal distribution, that is the result of a shift in the maxima over time, is also visible in the unsorted data (Figure 4-9). Method 2, having a set outer limit to the area being considered rather than an end of domain limit, excludes some of the outer rainbands. Given that the outer rainbands tend to have their maxima in the downshear-right quadrant, rather than the

downshear left like for the eyewall and inner rainbands (e.g. Corbosiero & Molinari, 2002; Hence & Houze, 2012), one could expect that method 1 would have more precipitation maxima downshear-left. However, this is not the case here. This would suggest that the orographic modification is outweighing the wind shear effect for the rainbands as Nesat approaches landfall. The intensity-sorted results are also similar to the results for method 1.

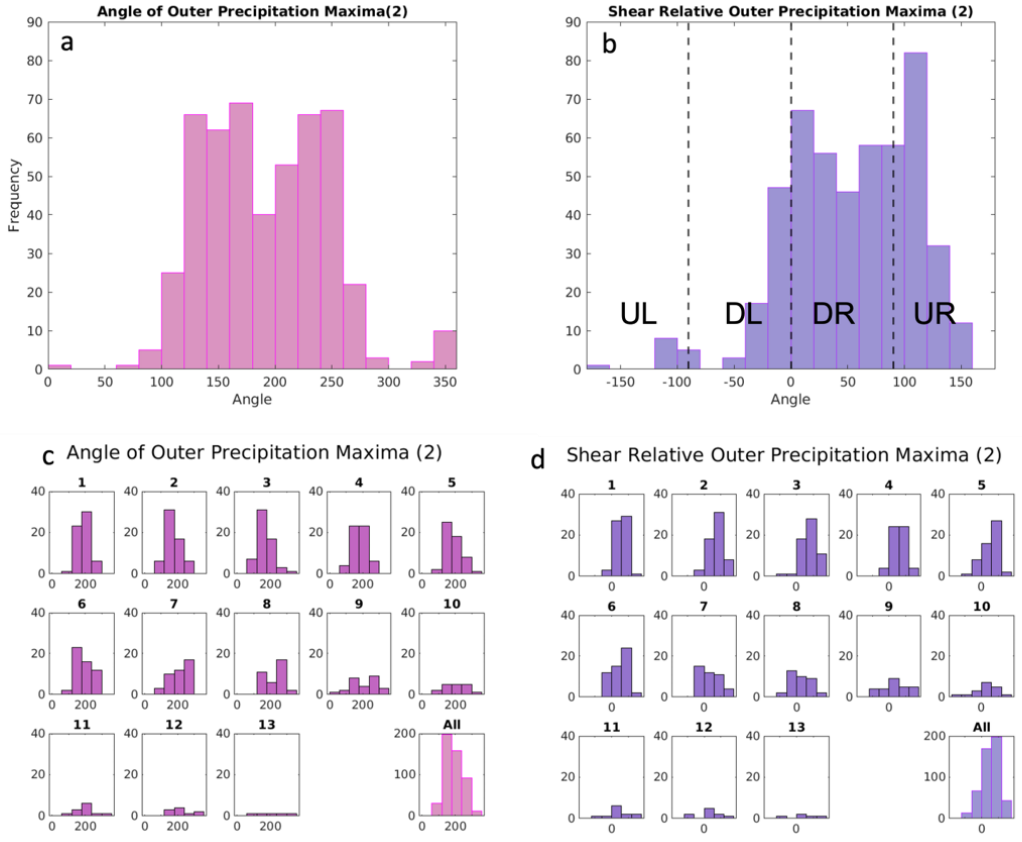

Figure **4-9**: Same as Figure 4-7 but for outer precipitation maxima (2).

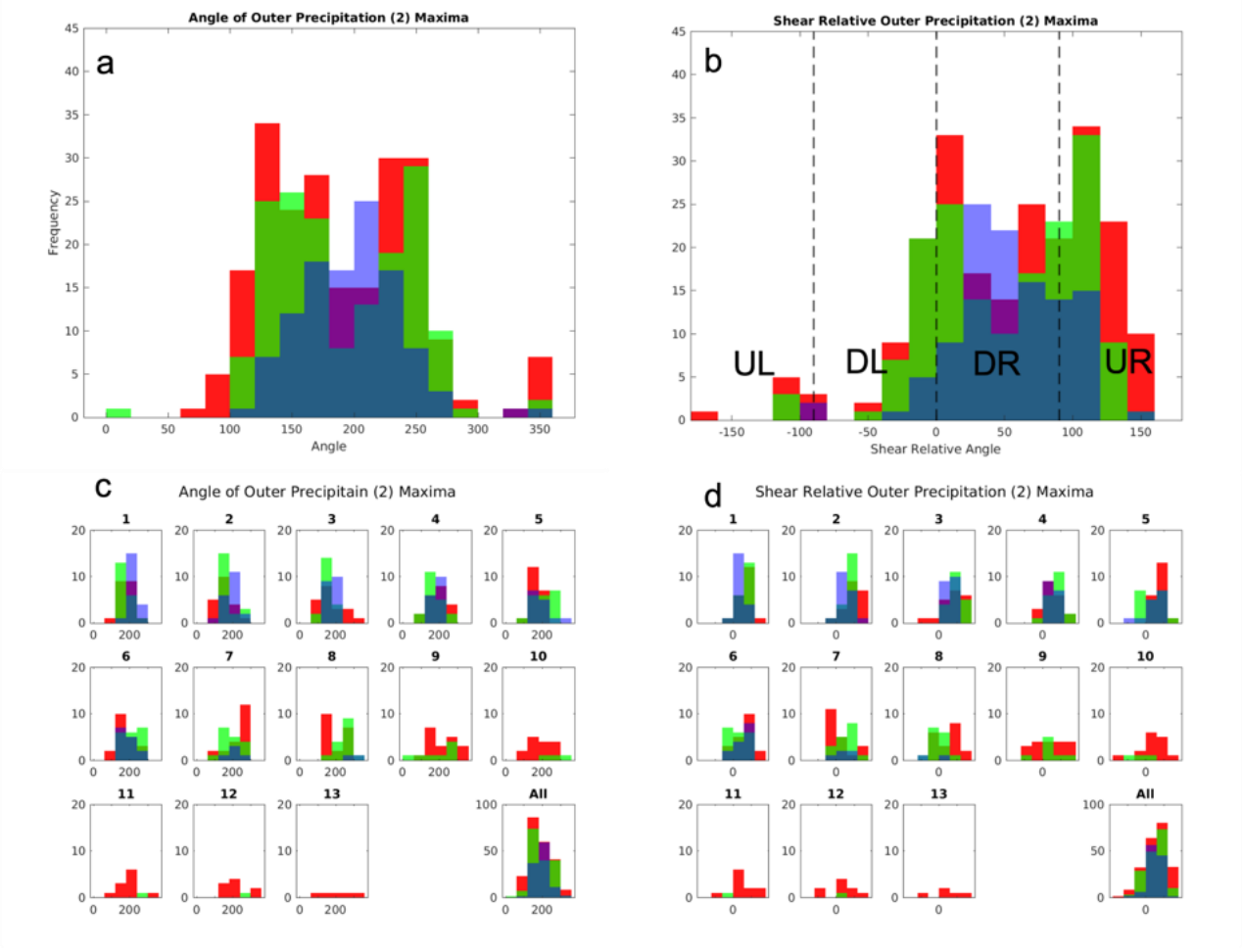

Figure **4-10**: Same as Figure 4-8 but for outer precipitation maxima (2).

Cross Section Analysis of TC Structures

In prior sections, the variability of the shear-aligned asymmetries in the eyewall and rainbands were examined for different storm intensities. To better analyze the characteristic structures and forcing mechanisms of the shear-aligned precipitation maxima, cross sections of the model data are analyzed. We focus on eyewall precipitation in ensemble members for the Strong and Weak categories; compared to rainband precipitation, eyewall precipitation had the most consistent signal of shear-relative location of maximum precipitation separated by intensity. The vertical structures of the wind and precipitation fields will be analyzed by intensity here in order to get a more complete analysis of the features associated with the precipitation maxima.

In order to look at the vertical structure, without the modification from landfall that was demonstrably happening in the prior section, the Strong and Weak categories were analyzed at the time halfway to landfall. For the ensemble members which reached landfall at an odd number of hours, the halfway point was rounded up to the closest hour. Composite cross sections were created to highlight any salient features across ensemble members within each group. To make these composites of storms with different sizes, the data was normalized by the RMW (also named r*). For each ensemble member the RMW was identified, the axis extended out to 10r* (higher axis values not included in figures due to a lack of data) and the data interpolated onto the new axis. This normalized data was then averaged together to get radius-height azimuthal averages of the following fields: tangential wind, radial wind, vertical wind, relative humidity (RH), snow mixing ratio, and rain mixing ratio.

Composites for the Strong and Weak storms are presented in Figure 4-11. As is visible in the figures, there is some vertical striping that is a result of the compositing. Where the normalized radius of the TC extended beyond the domain, any data from beyond the radius at the domain edge was not included in the compositing. The tangential wind composites confirm the structure of greater winds for the Strong storms and lesser winds for the Weak storms. Both categories have their maximum tangential winds at approximately 2 km altitude. The secondary circulation (radial and vertical velocities) follows the expected in-up-out pattern throughout most of the radii for both categories. The location of the strongest updrafts is at r* (the normalized RMW) within the eyewall for both categories, with the Strong group updraft being greater than that of the Weak. The Strong category's primary updraft has two local maxima around 6 km and 11 km altitude. Elevated updrafts are consistent with Heymsfield et al. (2010) who found that updraft maxima often occur above 10 km due to the latent heat of freezing providing buoyancy for the updrafts at upper levels. The updrafts at farther radii get progressively weaker as the storm gets weaker, and more downdrafts become apparent, particularly at 3.5r* radius and beyond. This finding is consistent with a storm's wind field being generally larger in size for stronger storms than for weaker storms and thus have axisymmetric updrafts from rainband activity that extend to farther radii. For both cases, relative humidity (RH) is highest at r* where the entire column is immersed in the eyewall cloud. For the Strong category, the RH column at r* has the higher values and is the widest, which is consistent with Wu et al.'s (2012) finding that RH increases with intensity. The Strong category also has the larger dip in RH between r* and the center of the storm between both categories, indicating that the more intense storms likely have the clearest eyes. The snow and rain mixing ratios' maxima are at r* for the Strong category and a bit inside r* for the Weak category, an additional indicator of higher intensity storms

having clearer eyes. The Strong category also has slightly higher rain mixing ratios, showing more intense precipitation in a specific spot in the eyewall region rather than the diffuse and less organized eyewalls of the Weak category, even though Figure 4-2 showed no eyewall rate differences. Overall the rain rate in the eyewall is similar for both categories, but the Strong category has more organized and localized heavy precipitation rather than the more diffuse precipitation of the Weak Category.

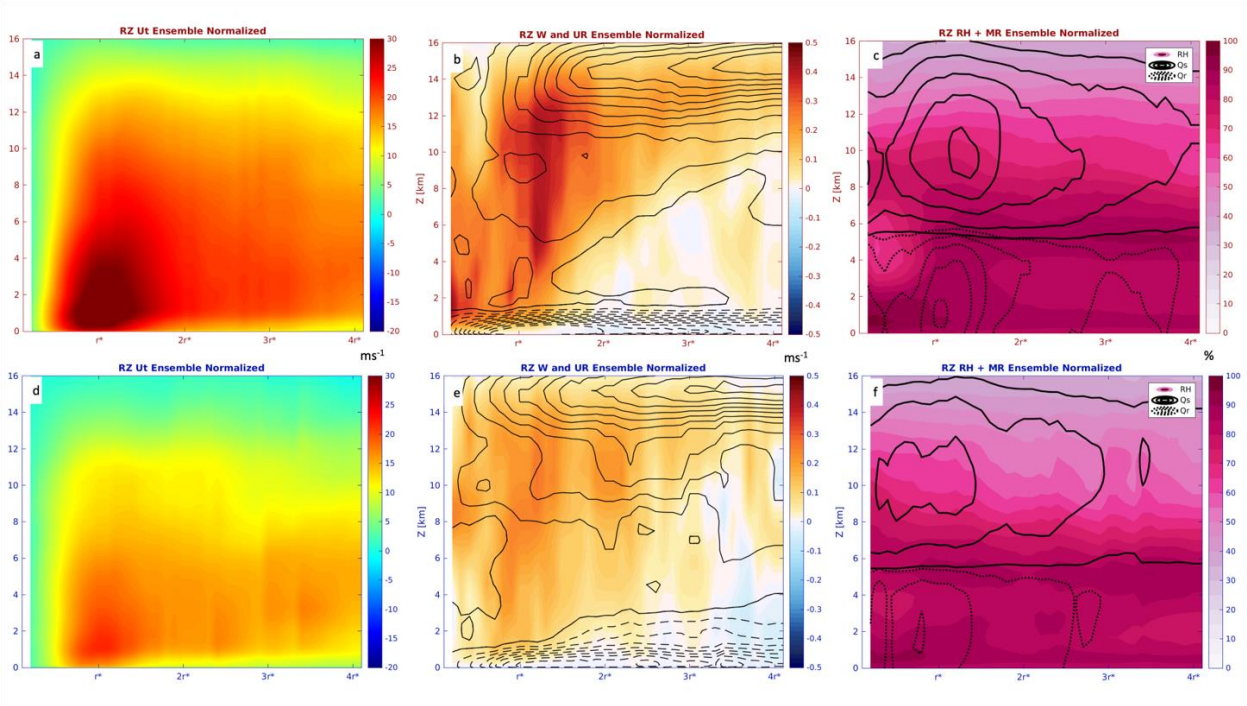

Figure **4-11**: The left hand column, a and d, shows the azimuthally averaged tangential wind as normalized by the RMW. The normalized radius is on the x-axis and height in km is on the y-axis. The middle column, b and e, displays the vertical wind speed in the colored contours. Reds are updrafts and blues are downdrafts. The dashed lines indicate inflow and the solid lines outflow. The right hand column, c and f, shows the relative humidity in the pink contours, the snow mixing ratio in the solid lines, and the rain mixing ratio in the dotted lines. The top row, a, b, c, is the Strong category, and the bottom row, d, e, f, is the Weak category.

In order to further examine the characteristic features that lead to peaks in eyewall precipitation, the vertical and radial wind patterns will be examined by quadrant relative to the angle of maximum eyewall precipitation (precip-max-relative quadrant) for both the Strong and Weak Categories. Figure 4-12 shows the precip-max-relative quadrant composites of vertical and radial wind averaged for the Strong category. In the quadrant 90° upwind of the angle of maximum precipitation (Figure 4-12b), the updrafts at the eyewall are stronger than the storm average, though they are in much the same place. Eyewall updraft strength peaks in this quadrant and becomes weaker downwind of the angle of maximum eyewall precipitation (Figure 4-12a,c,d). Here, the radial wind pattern outside the eyewall is generally inflow in the low and middle troposphere that feeds the deep updraft, and outflow that occurs in the upper troposphere. Moving downwind (Fig. 4-12a), the eyewall updraft remains strong, however its vertical extent is reduced. Instead of extending from near the surface to ~14 km, the strong updraft extends from ~7 km to ~14 km altitude. At the same time, downdrafts in this quadrant have the largest extent. They extend from just outside r* to 4r* and from near the surface up to ~8 km altitude, where the strong updraft starts. Inflow here now occurs in two layers: the boundary layer below 1 km and between 1.5-12 km. The deep inflow layer is no longer supporting a deep updraft. Instead, there is a deep layer of descending inflow that appears to erode the eyewall updraft in its lower half. Further downwind (Figure 4-12c), the radial flow changes to largely outflow. The downdraft present at low levels in the eyewall, in Figure 4-12c, is likely caused in part by precipitation drag (e.g., Cheng & Li, 2020; Zipser, 1977) from the heavy rainfall. The average shear direction is displayed by the red arrow in Fig. 4-12, pointing roughly 60° upwind of the maximum precipitation direction. Given that the angle of maximum precipitation is generally downshear-left, the quadrant 90° upwind of the angle of maximum precipitation approximately aligns with

downshear/downshear-right. Overall, the secondary circulation aligns well with previous studies on shear-relative asymmetries (e.g., Reasor et al., 2013). This is consistent with previous work showing that the strongest eyewall updrafts tend to be downshear with the heaviest precipitation

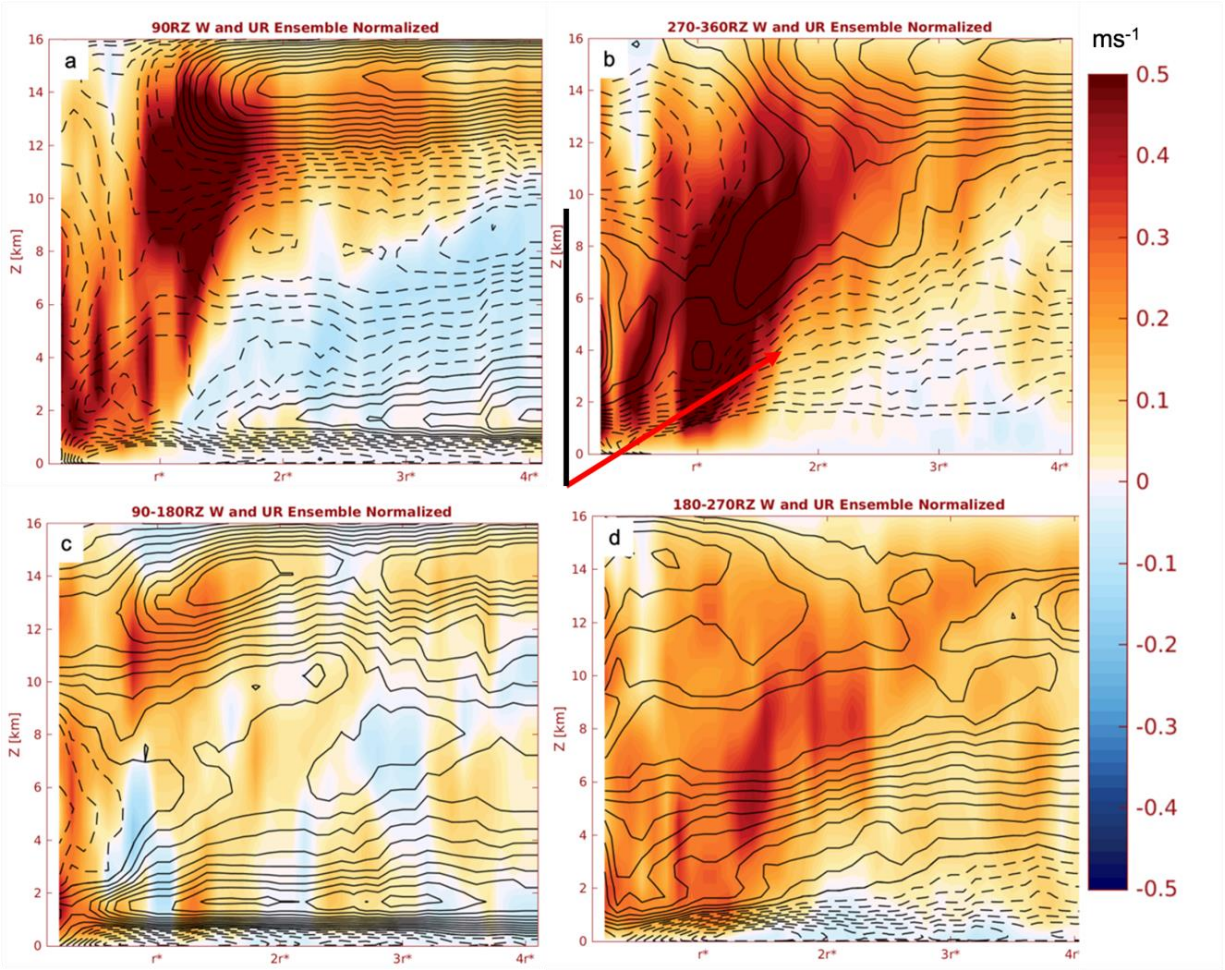

Figure **4-12**: The secondary circulation normalized by the RMW for each quadrant relative to maximum eyewall precipitation for the Strong category, a: 90° downwind, b: 90° upwind, c: 90°-180° downwind, d: 90°-180° upwind. The normalized radius is on the x-axis and height in km is on the y-axis. The vertical wind speed in the colored contours. Reds are updrafts and blues are downdrafts. The dashed lines indicate inflow and the solid lines outflow. The black line indicates maximum eyewall precipitation angle, the colored arrow indicates the shear direction.

being slightly downwind (e.g. Dehart et al., 2014), and the strongest rainband updrafts tend to be downshear-right (Barron et al., 2022). The secondary circulation is generally in-up-out in the downshear-left (same as in the quadrant 90° downwind of the angle of maximum precipitation) and downshear-right (quadrant 90° upwind of the angle of maximum precipitation), and the opposite quadrants have weaker vertical motions and predominant outflow above the boundary layer.

Figure 4-13 shows the secondary circulation by precip-max-relative quadrant for the Weak category. Overall the circulation is weaker than in the Strong category. The strongest updrafts are in the quadrant 90° upwind of the angle of maximum eyewall precipitation, (Figure 4-13b). In this composite, the local updraft maxima occur at both r* and 2r*, both of which are mostly above 6 km. There are downdrafts at lower levels from 3r* on out. Outside of the eyewall, there is inflow from the surface to ~8 km, and outflow above, leading to an overall in-up-out pattern. Moving to the quadrant 90° downwind (Figure 4-13a), the downdrafts are more widespread, the updrafts weaker, and the inflow extends up to 12 km, with some outflow at ~2 km altitude from 3r* to 4r*. This change is similar to the change that occurs between these quadrants in the strong case, though the updrafts are weaker, and the lower level outflow starts at a much higher radius. In the quadrant 90°-180° downwind (Figure 4-13c), the updrafts are at their weakest and are interspersed with downdrafts, both largely overlaid with radial outflow. The updrafts strengthen in the quadrant 90°-180° upwind (Figure 4-13d) of the angle of maximum eyewall precipitation, but, unlike in the Strong category composite, here the eyewall updraft is less organized and its updraft maximum is difficult to discern. In the Weak category, on average the angle of maximum precipitation is closer (~30°) to the shear direction than for the Strong category, consistent with Figure 4-6. The difference in shear and precip-max directions

certainly follows the finding in Figure 4-6 where the Strong category storms advect the heaviest precipitation further downwind from the shear-induced updraft. But the shear relative location of the vertical velocity structures are not clearly different between the two categories, likely because the difference in the shear angles is still small. Instead, the overall asymmetric pattern of the secondary circulation is still similar to that seen in the Strong category. The updrafts begin to form 90°-180° upwind of the angle of maximum precipitation, and then hit their full strength 90° upwind to form the heavy precipitation along the precip-max-angle direction. A strong upper-level updraft persists 90° downwind, and the weakest vertical velocities occur 90-180° downwind.

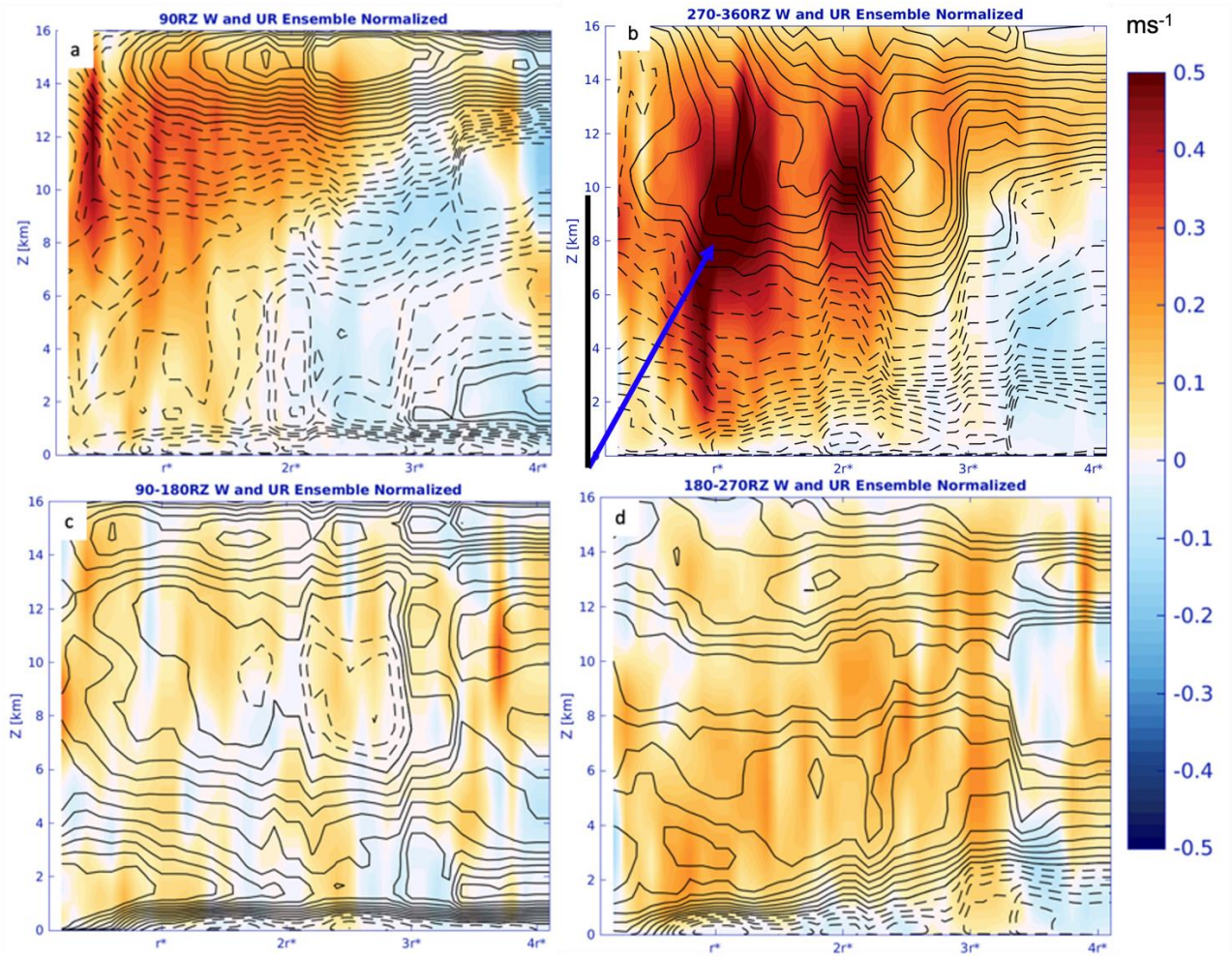

Figure **4-13**: Same as figure 4-12 but for the Weak category.

Chapter 5

Conclusions

We have analyzed the characteristics and variability of precipitation asymmetries in TCs using an ensemble model simulation of Typhoon Nesat (2017) that was run in preparation for the NSF PRECIP field campaign. The precipitation asymmetries in the eyewall and rainbands were analyzed by environmental vertical wind shear and by storm intensity at times leading to landfall in Taiwan. Environmental deep-layer (850-200 hPa) wind shear is a well-known factor in inducing asymmetries in a TC's kinematic and precipitation structures, but there remains much to be understood about the variability of these structures in real-case ensemble model forecasts, and how sensitive they are to small perturbations in initial conditions. This is important to examine because small shifts in storm intensity or structure can lead to dramatic variations in surface rainfall amounts, the understanding of which is the underlying motivation for the PRECIP field campaign. Most of the results presented here further support prior research in this field. However, the finding that hourly rain rate is insensitive to intensity, is counter to prior studies.

Our results showed that wind shear was linked to the location and intensity of eyewall precipitation asymmetries as well as the overall storm intensity. More intense storms tended to have lower shear magnitude and more precipitation, while less intense storms tended to have the opposite. While the one-hour rain rate did not vary with intensity, the rainfall accumulation during our time frame of interest (while the storm was over the open ocean) did. More intense

storms took longer to reach landfall on average, due to the differing influence of β-drift on the track trajectories, so more intense storms spent more time over the open ocean and thus had a larger accumulation of rain. Shear, however does change, which implies that the vertical wind shear does not have much effect on the rain rate.

While the vertical wind shear does not seem to effect rain rate it does effect rain location. As described in previous studies, the vertical wind shear tilts the vortex downshear/downshear-left, as shown by the maximum low-level PV generally being upshear-right. The tilt leads to a wavenumber-1 potential temperature anomaly that causes air to rise along the isentropes from the positive anomaly (uptilt, upshear-left) to the negative anomaly (downtilt, downshear-left). This places the maximum updrafts downshear right, whereupon the tangential winds advect the precipitation generated by this convection to the downshear-left. The stronger the storm (and the weaker the shear) the further the precipitation is advected.

Moving outwards to the rainbands, the convection is generated upshear right (e.g. Riemer, 2016) before being advected around the storm. Interestingly, a bimodal distribution of the maximum precipitation occurs, due to the rainbands making landfall and orographic effects shifting the precipitation maxima from its shear relative location, prior to the eyewall making landfall.

The secondary circulation can be helpful in elucidating where the precipitation is being generated. When examining the RZ plots of the secondary circulation, various structural elements were revealed. For example, the Strong storms had the strongest updrafts. They displayed the typical in-up-out pattern both overall, and in the quadrant upwind of the angle of maximum precipitation. Consistent with Dehart et al.'s (2014) finding that in the downshear left quadrant the secondary circulation is in-up-out and in, in the downshear right quadrant the

secondary circulation is in-up-out, and that the precipitation maxima is usually downshear left, the quadrants 90° above the angle of maximum eyewall precipitation show the in-up-out and in pattern for the secondary circulation for the normalized composites. However, it is less visible in the Weak category which is more in keeping with the downshear right in-up-out pattern consistent with the precipitation maxima for the weak category being closer to the shear.

Essentially, this work could aid in forecasting TC rainfall. Given that TC structure and thus rainfall is hard to predict, this additional information on the placement and intensity can be useful. Even looking from a precipitation relative standpoint the structures are in similar places relative to shear, adding more evidence that looking to shear for the placement of heavy precipitation in a TC is a valid approach. How the rate vs duration affects the total rainfall amount, with duration being of higher importance (at least in this case) shows that for forecasting, the track and expected duration of rainfall should likely be given more weight when deciding how much rain to expect.

Nevertheless, this study is limited in scope by only having one TC examined. More robust statistics could be gained from examining more TCs and/or having a larger ensemble size. Having a longer time period under consideration would help to separate out the orographic effects as the TC could be analyzed when further from landfall. Having a larger domain would prevent the necessity to remove ensemble members from the composites leading to fewer artifacts.

Future work to expand on this study could include doing a similar analysis with a larger domain size, with a TC further out from landfall in a similar location or to perform the same analysis on multiple TCs rather than just focusing on Nesat (2017). This could help improve the

understanding of the dynamics and the modeling and forecasting of TC precipitation, which is necessary to mitigate damage from the rainfall.

References

Barron, N. R., Didlake Jr., A. C., & Reasor, P. D. (2022). Statistical Analysis of Convective Updrafts in Tropical Cyclone Rainbands Observed by Airborne Doppler Radar. Journal of Geophysical Research: Atmospheres, 127(6), e2021JD035718. https://doi.org/10.1029/2021JD035718

Bender, M. A., Tuleya, R. E., & Kurihara, Y. (1987). A Numerical Study of the Effect of Island Terrain on Tropical Cyclones. *Monthly Weather Review*, *115*(1), 130–155. https://doi.org/10.1175/1520-0493(1987)115<0130:ANSOTE>2.0.CO;2

Bender, M. A. (1997). The Effect of Relative Flow on the Asymmetric Structure in the Interior of Hurricanes. *Journal of the Atmospheric Sciences*, *54*(6), 703–724. https://doi.org/10.1175/1520-0469(1997)054<0703:TEORFO>2.0.CO;2

Black, M. L., Gamache, J. F., Marks, F. D., Samsury, C. E., & Willoughby, H. E. (2002), Eastern Pacific Hurricanes Jimena of 1991 and Olivia of 1994: The Effect of Vertical Shear on Structure and Intensity. *Monthly Weather Review*, 130(9), 2291–2312. https://doi.org/10.1175/1520-0493(2002)130<2291:EPHJOA>2.0.CO;2

Boehm, A. M., & Bell, M. M. (2021). Retrieved Thermodynamic Structure of Hurricane Rita (2005) from Airborne Multi–Doppler Radar Data. *Journal of the Atmospheric Sciences, 78*(5), 1583–1605. https://doi.org/10.1175/JAS-D-20-0195.1

Braun, S. A., Montgomery, M. T., & Pu, Z. (2006), High-Resolution Simulation of Hurricane Bonnie (1998). Part I: The Organization of Eyewall Vertical Motion. *Journal of the Atmospheric Sciences*, 63(1), 19–42. https://doi.org/10.1175/JAS3598.1

Brown, B. R., Bell, M. M., & Frambach, A. J. (2016). Validation of simulated hurricane drop size distributions using polarimetric radar. *Geophysical Research Letters, 43*(2), 910–917. https://doi.org/10.1002/2015GL067278

Chan, J. C. L., & Williams, R. T. (1987). Analytical and Numerical Studies of the Beta-Effect in Tropical Cyclone Motion. Part I: Zero Mean Flow. *Journal of the Atmospheric Sciences, 44*(9), 1257–1265. https://doi.org/10.1175/1520-0469(1987)044<1257:AANSOT>2.0.CO;2

Chen, S. S., Knaff, J. A., & Marks, F. D. (2006). Effects of Vertical Wind Shear and Storm Motion on Tropical Cyclone Rainfall Asymmetries Deduced from TRMM. *Monthly Weather Review,* 134(11), 3190–3208. https://doi.org/10.1175/MWR3245.1

Cheng, J., & Li, Q. (2020). A numerical study of convective-scale downdrafts in the outer core of tropical cyclones in vertically varying environmental flows. *Tropical Cyclone Research and Review*, 9(3), 143–161. https://doi.org/10.1016/j.tcrr.2020.06.002

Corbosiero, K. L., & Molinari, J. (2002). The Effects of Vertical Wind Shear on the Distribution of Convection in Tropical Cyclones. *Monthly Weather Review*, 130(8), 2110–2123. https://doi.org/10.1175/1520-0493(2002)130<2110:TEOVWS>2.0.CO;2

Corbosiero, K. L., & Molinari, J. (2003), The Relationship between Storm Motion, Vertical Wind Shear, and Convective Asymmetries in Tropical Cyclones. *Journal of Atmospheric Sciences*, 60(2), 366–376. https://doi.org/10.1175/1520-0469(2003)060<0366:TRBSMV>2.0.CO;2

Davis, C., Snyder, C., & Didlake, A. C. (2008). A Vortex-Based Perspective of Eastern Pacific Tropical Cyclone Formation. *Monthly Weather Review*, 136(7), 2461–2477. https://doi.org/10.1175/2007MWR2317.1

DeHart, J. C., Houze, R. A., & Rogers, R. F. (2014). Quadrant Distribution of Tropical Cyclone Inner-Core Kinematics in Relation to Environmental Shear. *Journal of the Atmospheric Sciences*, 71(7), 2713–2732. https://doi.org/10.1175/JAS-D-13-0298.1

DeMaria, M. (1996). The Effect of Vertical Shear on Tropical Cyclone Intensity Change. *Journal of the Atmospheric Sciences*, *53*(14), 2076–2088. https://doi.org/10.1175/1520-0469(1996)053<2076:TEOVSO>2.0.CO;2

Didlake, A. C., & Houze, R. A. (2013). Dynamics of the Stratiform Sector of a Tropical Cyclone Rainband. *Journal of the Atmospheric Sciences*, *70*(7), 1891–1911. https://doi.org/10.1175/JAS-D-12-0245.1

Didlake, A. C., & Kumjian, M. R. (2017). Examining Polarimetric Radar Observations of Bulk Microphysical Structures and Their Relation to Vortex Kinematics in Hurricane Arthur (2014). *Monthly Weather Review*, *145*(11), 4521–4541. https://doi.org/10.1175/MWR-D-17-0035.1

Doswell, C. A., Brooks, H. E., & Maddox, R. A. (1996). Flash Flood Forecasting: An Ingredients-Based Methodology. *Weather and Forecasting*, 11(4), 560–581. https://doi.org/10.1175/1520-0434(1996)011<0560:FFFAIB>2.0.CO;2

Feng, Y.-C., & Bell, M. M. (2019). Microphysical Characteristics of an Asymmetric Eyewall in Major Hurricane Harvey (2017). *Geophysical Research Letters*, *46*(1), 461–471. https://doi.org/10.1029/2018GL080770

Frank, W. M., & Ritchie, E. A. (1999), Effects of Environmental Flow upon Tropical Cyclone Structure. *Monthly Weather Review*, 127(9), 2044–2061. https://doi.org/10.1175/1520-0493(1999)127<2044:EOEFUT>2.0.CO;2

Frank, W. M., & Ritchie, E. A. (2001). Effects of Vertical Wind Shear on the Intensity and Structure of Numerically Simulated Hurricanes. *Monthly Weather Review*, *129*(9), 2249–2269. https://doi.org/10.1175/1520-0493(2001)129<2249:EOVWSO>2.0.CO;2

Gray, W. M. (1968). Global View of the Origin of Tropical Disturbances and Storms. Monthly Weather Review, 96(10), 669–700. https://doi.org/10.1175/1520-0493(1968)096<0669:GVOTOO>2.0.CO;2

Gu, J.-F., Tan, Z.-M., & Qiu, X. (2015). Effects of Vertical Wind Shear on Inner-Core Thermodynamics of an Idealized Simulated Tropical Cyclone. *Journal of the Atmospheric Sciences*, *72*(2), 511–530. https://doi.org/10.1175/JAS-D-14-0050.1

Han, Y, Delst, P. van, Liu, Q., Weng, F., Yan, B., Treadon, R., & Derber, J. (2006). JCSDA Community Radiative Transfer Model (CRTM)—version 1. NOAA Tech. Rep. NESDIS 122, 40 pp.

Hence, D. A., & Houze, R. A. (2011). Vertical Structure of Hurricane Eyewalls as Seen by the TRMM Precipitation Radar. *Journal of the Atmospheric Sciences*, 68(8), 1637–1652. https://doi.org/10.1175/2011JAS3578.1

Hence, D. A., & Houze, R. A. (2012). Vertical Structure of Tropical Cyclone Rainbands as Seen by the TRMM Precipitation Radar. *Journal of the Atmospheric Sciences*, 69(9), 2644–2661. https://doi.org/10.1175/JAS-D-11-0323.1

Heymsfield, G. M., Tian, L., Heymsfield, A. J., Li, L., & Guimond, S. (2010). Characteristics of Deep Tropical and Subtropical Convection from Nadir-Viewing High-Altitude Airborne Doppler Radar. *Journal of the Atmospheric Sciences,* 67(2), 285–308. https://doi.org/10.1175/2009JAS3132.1

Hong, S., Noh, Y., & Dudhia, J. (2006). A New Vertical Diffusion Package with an Explicit Treatment of Entrainment Processes, *Monthly Weather Review*, 134(9), 2318-2341.

Houtekamer, P. L., & Mitchell, H. L. (2001). A sequential ensemble Kalman filter for atmospheric data assimilation. *Monthly Weather Review*, 129(1), 123–137.

Houze Jr., R. A. (2012). Orographic effects on precipitating clouds. *Reviews of Geophysics*, 50(1). https://doi.org/10.1029/2011RG000365

Houze, R. A. (2010), Clouds in Tropical Cyclones. *Monthly Weather Review*, 138(2), 293–344. https://doi.org/10.1175/2009MWR2989.1

Huang, C.-Y., Chen, C.-A., Chen, S.-H., & Nolan, D. S. (2016). On the Upstream Track Deflection of Tropical Cyclones Past a Mountain Range: Idealized Experiments. *Journal of the Atmospheric Sciences*, *73*(8), 3157–3180. https://doi.org/10.1175/JAS-D-15-0218.1

Huang, C.-Y., Huang, C.-H., & Skamarock, W. C. (2019). Track Deflection of Typhoon Nesat (2017) as Realized by Multiresolution Simulations of a Global Model. *Monthly Weather Review*, *147*(5), 1593–1613. https://doi.org/10.1175/MWR-D-18-0275.1

Iacono, M. J., Delamere, J. S., Mlawer, E. J., Shephard, M. W., Clough, S. A., & Collins, W. D. (2008). Radiative forcing by long-lived greenhouse gases: Calculations with the AER radiative transfer models. *Journal of Geophysical Research: Atmospheres*, 113(D13), D13103.

Jiménez, P. A., Dudhia, J., González-Rouco, J. F., Navarro, J., Montávez, J. P., & García-Bustamante, E. (2012). A revised scheme for the WRF surface layer formulation, *Monthly Weather Review*, 140(3), 898–918.

Jones, S. C. (1995). The evolution of vortices in vertical shear. I: Initially barotropic vortices. *Quarterly Journal of the Royal Meteorological Society*, *121*(524), 821–851. https://doi.org/10.1002/qj.49712152406

Knapp, K. R., Kruk, M. C., Levinson, D. H., Diamond, H. J., & Neumann, C. J. (2010). The International Best Track Archive for Climate Stewardship (IBTrACS): Unifying Tropical Cyclone Data. *Bulletin of the American Meteorological Society*, *91*(3), 363–376. https://doi.org/10.1175/2009BAMS2755.1

Knapp, K. R., Velden, C. S., & Wimmers, A. J. (2018). A Global Climatology of Tropical Cyclone Eyes. *Monthly Weather Review*, *146*(7), 2089–2101. https://doi.org/10.1175/MWR-D-17-0343.1

Lonfat, M., Marks, F. D., Jr., & Chen, S. S. (2004). Precipitation Distribution in Tropical Cyclones Using the Tropical Rainfall Measuring Mission (TRMM) Microwave Imager: A Global Perspective, *Monthly Weather Review*, 132(7), 1645-1660. 10.1175/1520-0493(2004)132<1645:PDITCU>2.0.CO;2

Marks, F. D., & Houze, R. A. (1987), Inner Core Structure of Hurricane Alicia from Airborne Doppler Radar Observations. *Journal of the Atmospheric Scienc*es, 44(9), 1296–1317. https://doi.org/10.1175/1520-0469(1987)044<1296:ICSOHA>2.0.CO;2

Merrill, R. T. (1988). Environmental Influences on Hurricane Intensification. *Journal of the Atmospheric Sciences*, *45*(11), 1678–1687. https://doi.org/10.1175/1520-0469(1988)045<1678:EIOHI>2.0.CO;2

Morrison, H., van Lier-Walqui, M., Fridlind, A. M., Grabowski, W. W., Harrington, J. Y., Hoose, C., et al. (2020), Confronting the Challenge of Modeling Cloud and Precipitation Microphysics. *Journal of Advances in Modeling Earth Systems*, 12(8), e2019MS001689. https://doi.org/10.1029/2019MS001689

Nguyen, L. T., Molinari, J., & Thomas, D. (2014). Evaluation of Tropical Cyclone Center Identification Methods in Numerical Models. *Monthly Weather Review*, 142(11), 4326–4339. https://doi.org/10.1175/MWR-D-14-00044.1

PRECIP 2022 Science. (n.d.). Retrieved May 22, 2022, from http://precip.org/science/

Rappaport, E. N. (2014), Fatalities in the United States from Atlantic Tropical Cyclones: New Data and Interpretation. *Bulletin of the American Meteorological Society*, 95(3), 341– 346. https://doi.org/10.1175/BAMS-D-12-00074.1

Reasor, P. D., Rogers, R., & Lorsolo, S. (2013), Environmental Flow Impacts on Tropical Cyclone Structure Diagnosed from Airborne Doppler Radar Composites. *Monthly Weather Review*, 141(9), 2949–2969. https://doi.org/10.1175/MWR-D-12-00334.1

Riemer, M. (2016). Meso-β-scale environment for the stationary band complex of vertically sheared tropical cyclones. *Quarterly Journal of the Royal Meteorological Society*, *142*(699), 2442–2451. https://doi.org/10.1002/qj.2837

Shapiro, L. J. (1983), The Asymmetric Boundary layer Flow Under a Translating Hurricane. *Journal of the Atmospheric Sciences*, 40(8), 1984–1998. https://doi.org/10.1175/1520-0469(1983)040<1984:TABLFU>2.0.CO;2

Skamarock, W. C., Klemp, J. B., Dudhia, J., Gill, D. O., Liu, Z., Berner, J., et al. (2019). *A Description of the Advanced Research WRF Model Version 4*. UCAR/NCAR. https://doi.org/10.5065/1DFH-6P97

Smith, R. B., Schafer, P., Kirshbaum, D., & Regina, E. (2009). Orographic Enhancement of Precipitation inside Hurricane Dean. *Journal of Hydrometeorology*, 10(3), 820–831. https://doi.org/10.1175/2008JHM1057.1

Sukovich, E. M., Ralph, F. M., Barthold, F. E., Reynolds, D. W., & Novak, D. R. (2014), Extreme Quantitative Precipitation Forecast Performance at the Weather Prediction Center from 2001 to 2011. *Weather and Forecasting*, 29(4), 894–911. https://doi.org/10.1175/WAF-D-13-00061.1

Tewari, M., Chen, F., Wang, W., Dudhia, J., LeMone, M. A., Mitchell, K., Ek, M., Gayno, G., Wegiel, J., & Cuenca, R. H. (2004). Implementation and verification of the unified NOAH land surface model in the WRF model. 20th conference on weather analysis and forecasting/16th conference on numerical weather prediction, pp. 11–15.

Thompson, G., & Eidhammer, T. (2014). A Study of aerosol impacts on clouds and precipitation development in a large winter cyclone. *Journal of the Atmospheric Sciences*, 71(10), 3636–3658.

Uhlhorn, E. W., Klotz, B. W., Vukicevic, T., Reasor, P. D., & Rogers, R. F. (2014). Observed Hurricane Wind Speed Asymmetries and Relationships to Motion and Environmental Shear. *Monthly Weather Review*, 142(3), 1290–1311. https://doi.org/10.1175/MWR-D-13-00249.1

Wang, B., & Li, X. (1992). The Beta Drift of Three-Dimensional Vortices: A Numerical Study. *Monthly Weather Review*, *120*(4), 579–593. https://doi.org/10.1175/1520-0493(1992)120<0579:TBDOTD>2.0.CO;2

Wang, Y., & Holland, G. J. (1996). The Beta Drift of Baroclinic Vortices. Part I: Adiabatic Vortices. *Journal of the Atmospheric Sciences*, *53*(3), 411–427. https://doi.org/10.1175/1520-0469(1996)053<0411:TBDOBV>2.0.CO;2

Willoughby, H. E., Marks, F. D., & Feinberg, R. J. (1984). Stationary and Moving Convective Bands in Hurricanes. *Journal of the Atmospheric Sciences*, 41(22), 3189–3211. https://doi.org/10.1175/1520-0469(1984)041<3189:SAMCBI>2.0.CO;2

Wingo, M. T., & Cecil, D. J. (2010). Effects of Vertical Wind Shear on Tropical Cyclone Precipitation. *Monthly Weather Review*, *138*(3), 645–662. https://doi.org/10.1175/2009MWR2921.1

Wong, M. L. M., & Chan, J. C. L. (2004). Tropical Cyclone Intensity in Vertical Wind Shear. *Journal of the Atmospheric Sciences*, *61*(15), 1859–1876. https://doi.org/10.1175/1520-0469(2004)061<1859:TCIIVW>2.0.CO;2

Wu, C.-C. (2001). Numerical Simulation of Typhoon Gladys (1994) and Its Interaction with Taiwan Terrain Using the GFDL Hurricane Model. *Monthly Weather Review*, *129*(6), 1533–1549. https://doi.org/10.1175/1520-0493(2001)129<1533:NSOTGA>2.0.CO;2

Wu, L., Su, H., Fovell, R. G., Wang, B., Shen, J. T., Kahn, B. H., et al. (2012). Relationship of environmental relative humidity with North Atlantic tropical cyclone intensity and intensification rate. *Geophysical Research Letters*, *39*(20). https://doi.org/10.1029/2012GL053546

Wu, M., Wu, C.-C., Yen, T.-H., & Luo, Y. (2017). Synoptic Analysis of Extreme Hourly Precipitation in Taiwan during 2003–12. *Monthly Weather Review*, 145(12), 5123–5140. https://doi.org/10.1175/MWR-D-17-0230.1

Xu, W., Jiang, H., & Kang, X. (2014). Rainfall asymmetries of tropical cyclones prior to, during, and after making landfall in South China and Southeast United States. *Atmospheric Research*, 139, 18–26. https://doi.org/10.1016/j.atmosres.2013.12.015

Yang, L., Fei, J., Huang, X., Cheng, X., Yang, X., Ding, J., & Shi, W. (2016). Asymmetric distribution of convection in tropical cyclones over the western North Pacific Ocean. *Advances in Atmospheric Sciences*, 33(11), 1306–1321. https://doi.org/10.1007/s00376-016-5277-x

Yeh, T.-C., & Elsberry, R. L. (1993). Interaction of Typhoons with the Taiwan Orography. Part I: Upstream Track Deflections. *Monthly Weather Review*, *121*(12), 3193–3212. https://doi.org/10.1175/1520-0493(1993)121<3193:IOTWTT>2.0.CO;2

Yu, Z., Wang, Y., & Xu, H. (2015), Observed Rainfall Asymmetry in Tropical Cyclones Making Landfall over China. *Journal of Applied Meteorology and Climatology*, 54(1), 117–136. https://doi.org/10.1175/JAMC-D-13-

Yu, Z., Wang, Y., Xu, H., Davidson, N., Chen, Y., Chen, Y., & Yu, H. (2017). On the Relationship between Intensity and Rainfall Distribution in Tropical Cyclones Making Landfall over China. *Journal of Applied Meteorology and Climatology*, *56*(10), 2883–2901. https://doi.org/10.1175/JAMC-D-16-0334.1

Zipser, E. J. (1977). Mesoscale and Convective–Scale Downdrafts as Distinct Components of Squall-Line Structure. *Monthly Weather Review*, 105(12), 1568–1589. https://doi.org/10.1175/1520-0493(1977)105<1568:MACDAD>2.0.CO;2